Electronic Supplementary Information

1 Particle size distributions of PI-Kem NMC811 and Timcal SuperC65 carbon black

NMC811 readily disperses in water, which is the medium used for the Malvern Mastersizer 3000 used to measure particle size distributions on the order of 0.1-10 μm (see Fig. 1). The volume-average hydrodynamic radius of NMC is 13 μm. CB is also sonicated in water, but the average particle size indicates significant agglomeration.

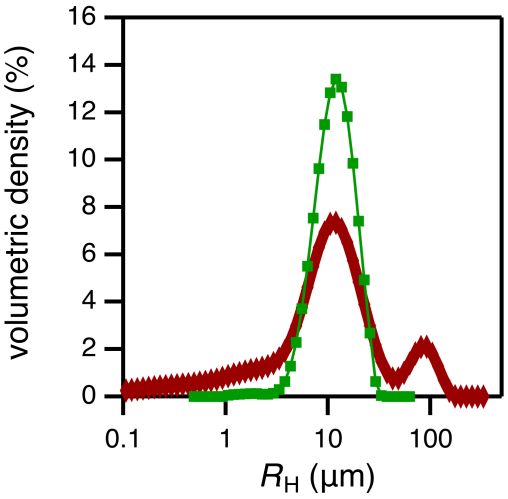

Figure 1 Particle size distributions of NMC (■) and CB (♦) in water measured by a Malvern Mastersizer 3000. The volume-averaged hydrodynamic radius is given as R_H.

Carbon black is hydrophobic and does not readily disperse in water, but has been reported to disperse in NMP[1]. A dispersion of 0.087 wt% CB in NMP is sonicated for sequential amounts of time and the hydrodynamic radius is measured using dynamic light scattering (DLS), which is more suitable than the Mastersizer for sub-micron scale particles (see Fig. 2). The viscosity-averaged hydrodynamic radius continues to drop with sonication, reaching 550 nm after 90 min. This size is still significantly greater than the reported secondary fractal size of 150 nm[2], indicating that the CB is not fully deagglomerated by this processing.

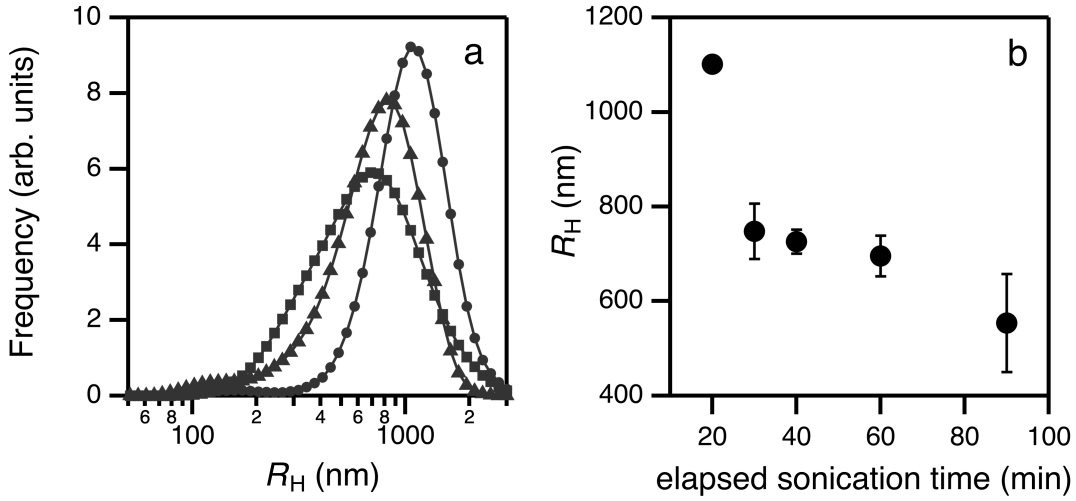

Figure 2 Particle size of CB in NMP measured by DLS following sonication for different time increments. a) Volume-weighted particle size distribution for time increments as noted in the legend. b) Viscosity-averaged hydrodynamic radius, R_H. Error bars denote half the difference between the volume-averaged and viscosity-averaged radii.

2 PVDF coil dimensions in NMP

Polymer chains adopt a random coil configuration in a good solvent to maximise the number of solvent–monomer interactions. The Flory–Huggins interaction parameter for PVDF in NMP was quantified by Lutringer and Weiss in 1991 using light scattering and inverse gas chromatography[3] and they report an average value of $\chi_{1,2} = 0.1 \pm 0.05$ and $\chi_{1,2} = -1.5$, respectively. Okabe *et al.*[4] made similar measurements using inverse gas chromatography in 2003 and report $\chi_{1,2}$ values between -0.5 and -1 for temperatures on the range of 130–225°C. These results both indicate that NMP is a good solvent for PVDF. The expected relationship between the chain dimension and the molecular weight of the polymer is

$$R_N \sim N^{\nu} \tag{1}$$

where R_N is the ensemble-averaged end-to-end distance between the first and last monomer in a chain, N is the number of polymer units and ν is an exponent related to solvent quality. For a good solvent, $\nu = 0.588$.

The calculation of N depends on the definition of a polymer unit, which changes when chains are renormalised, e.g. as an equivalent freely jointed chain. We were unable to find the Kuhn segment length or characteristic ratio for PVDF, so we will choose N to be the number of monomer units, hereafter denoted N_{mon} for clarity, where $N_{mon} = \bar{M}_w / M_{mon}$. The molecular weight of a PVDF monomer is given by $M_{mon} = 44.0$ g mol^{-1}.

Dynamic light scattering (DLS) was used to measure the hydrodynamic radius of 1 wt% PVDF samples in NMP. Measurements were attempted for all samples, but only H15 and H320 dissolved completely, yielding meaningful data. The DLS measurements are shown in Table 1.

Table 1 Measured PVDF radii of gyration, R_g, in NMP

polymer label	R_h (nm)
H15	9.5 ± 0.5
H320	27.9 ± 1.9

We use the measured hydrodynamic radius to approximate R_N, which is appropriate given that both values are actually chords describing coil dimensions rather than the radius of a sphere. From the measured values in Table 1 and Eqn. 1 we obtain an experimental value $\nu = 0.545$, well within the expected limit for a good solvent. The constant of proportionality in Eqn. 1 would generally depend upon the Kuhn segment length and the characteristic ratio for the polymer, neither of which are known. Lumping these together, we calculate a constant of proportionality for solutions of PVDF in NMP and can write the relationship

$$R_N = 0.102 N_{mon}^{0.545}. \tag{2}$$

This expression was used to estimate the values of R_h (see Table 2) for polymer samples that were too hazy to yield DLS results.

3 Viscosity–composition calibration for blends of H320 and H15

Blends of the two homopolymer solutions with the highest and lowest viscosities, 316 and 15 mPa·s, respectively, were prepared to smoothly access intermediate viscosities. Blends were also used to replicate the viscosities of homopolymer solutions. The viscosity of a series of blends was measured using capillary viscometry and used to construct a calibration plot (see Fig. 3) correlating viscosity with the composition of the blend. Regardless of the blending ratio, all blends comprised 3.9 wt% PVDF in NMP.

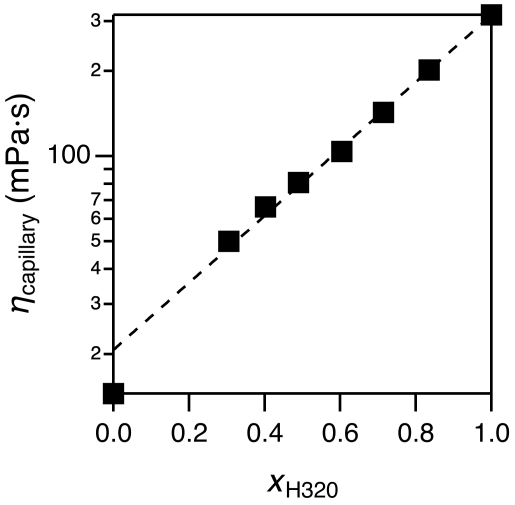

Figure 3 Dynamic viscosity as a function of the weight fraction of H320 in the solution. The fitted logarithmic relationship is given by $y = 20.7 \times 10^{1.18x}$.

4 Composition of each type of dispersion studied

Three types of dispersions were prepared from each polymer solution with mass fractions listed in Table 2.

Table 2 Mass fraction of each component for the three types of dispersions studied

Species	NMC dispersion	CB dispersion	cathode slurry
NMC	0.418	—	0.409
CB	—	0.038	0.023
PVDF	0.023	0.038	0.023
NMP	0.559	0.923	0.546

5 Viscosity of homopolymer solutions of PVDF

The viscosity of 3.9 wt% solutions of PVDF in NMP is measured using both rotational and capillary viscometry for each of the six purchased samples of PVDF. Flow curves measured using rotational viscosity are shown in Fig. 4a. The low frequency data are truncated due to noise. At high frequencies, the high molecular-weight samples are shear thinning due to the breakup of chain entanglements. The Newtonian plateau is fitted with a zero-slope line to determine the viscosity of the sample.

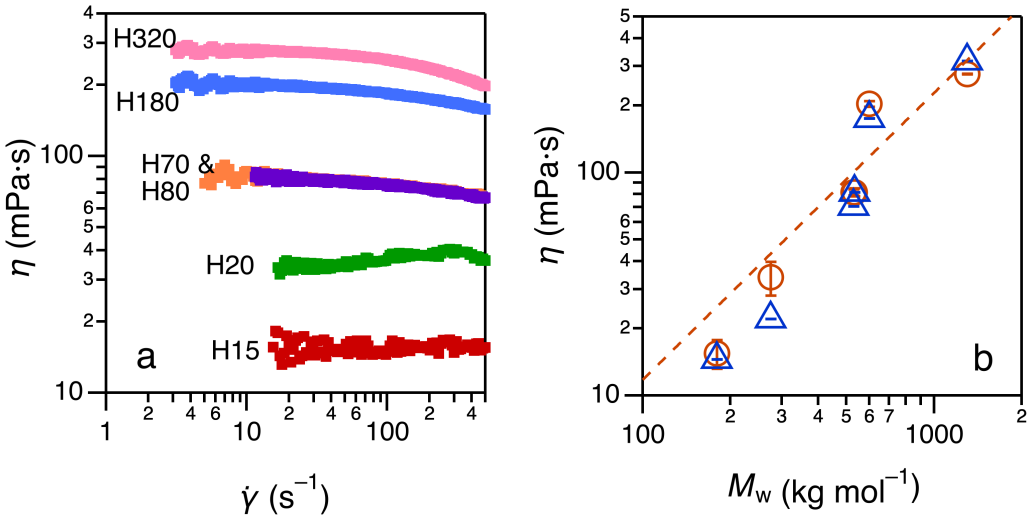

Figure 4 a) Viscosity flow curves for a series of homopolymer solutions comprising 3.9 wt% PVDF in NMP. The molecular weight of the PVDF is varied, giving rise to different solution viscosities. Samples are labelled on the plot as Hxx, where xx is the capillary viscosity of the solution in mPa·s. The molecular weight of the PVDF sample is: 180 kg mol^{-1} (H15), 275 kg mol^{-1} (H22), 530 kg mol^{-1} (H70), 534 kg mol^{-1} (H71), 600 kg mol^{-1} (H175) and 1,300 kg mol^{-1} (H316). b) Dynamic viscosity of solutions of 3.9 wt% PVDF in NMP measured using capillary viscometry (△) and rotational viscometry (○). The dashed line is a power-law fit to the capillary viscometry data illustrating an approximation of the Mark–Houwink relationship: $\eta = 0.0315 M_w^{1.29}$

To validate the somewhat noisy rotational viscometry measurements, the samples are also measured using capillary viscometry, which is suitable for the lower viscosity of the polymer solutions. Both measured values of viscosity are plotted against the manufacturer's stated molecular weight in Fig. 4b. The expected power-law relationship is evident and the datasets agree reasonably well. Noise around the power-law fit shown is likely due to variations in the polydispersity of the homopolymer samples and chain architecture, e.g. branching and tacticity.

6 Viscosity flow curves for CB dispersions and NMC cathode slurries

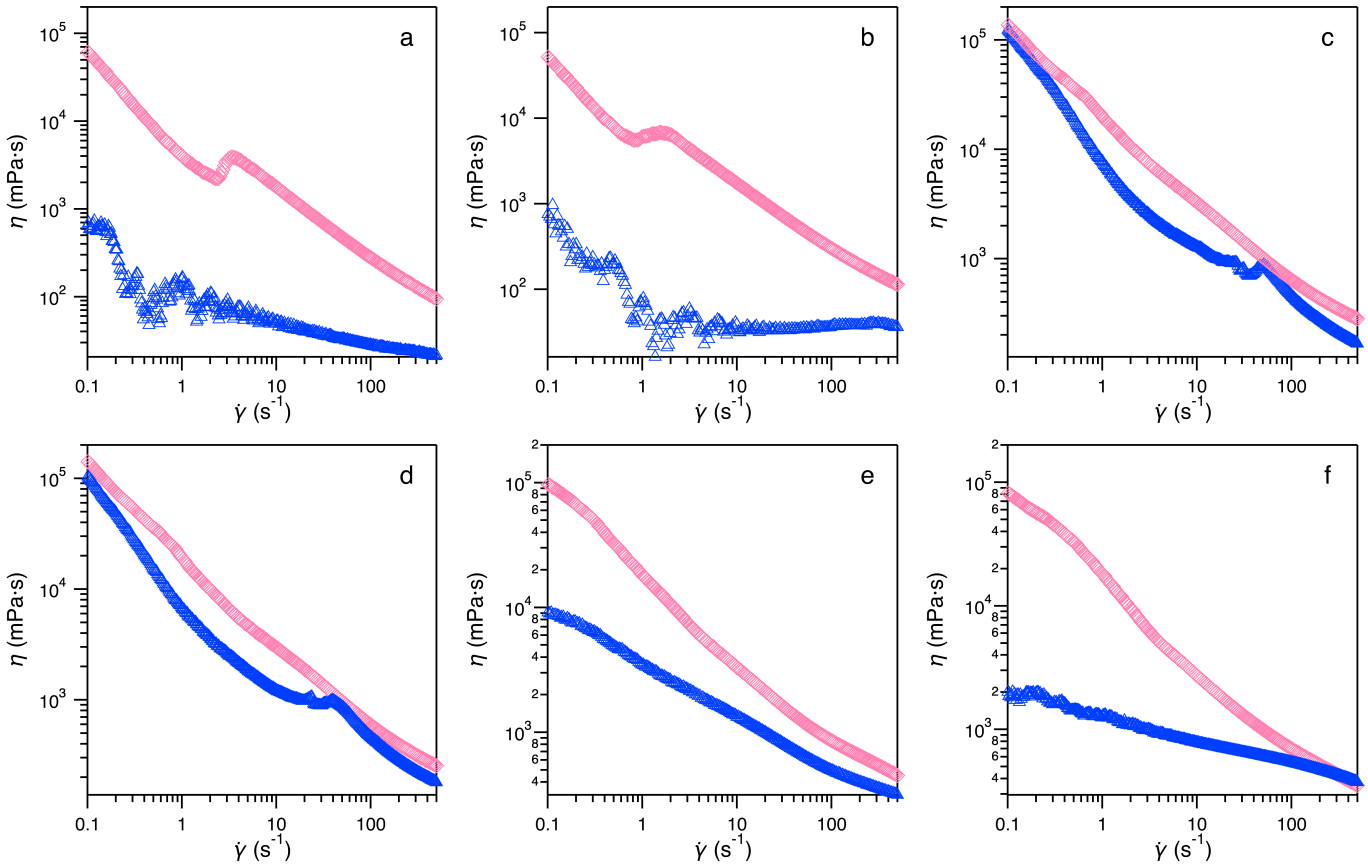

Figure 5 Rotational viscometry data for solid dispersions in solutions of 3.9 wt% PVDF in NMP. Dispersions of CB in 1:1 w/w ratio with PVDF (◇) and cathode slurries of NMC811/CB/PVDF in the ratio 95:5:5 and 43 wt% solids loading (△). Samples are named Hxx where xx is the viscosity of the PVDF/NMP solution in mPa·s: a) H15, b) H20, c) H70, d) H80, e) H180 and f) H320.

7 Control measurement of centrifuged PVDF solutions

Slurries were centrifuged to remove CB and NMC, and the viscosity of the supernatant was used to determine that amount of PVDF associated with the solids. A control was carried out to ensure that centrifugation was not precipitating the polymer coils from solution. The viscosity at a strain rate of 100 s^{-1} was measured for each homopolymer PVDF solution before and after centrifugation (see Fig. 6). There is no significant change for most of the polymer solutions measured; however, there is a slight loss of PVDF in H180.

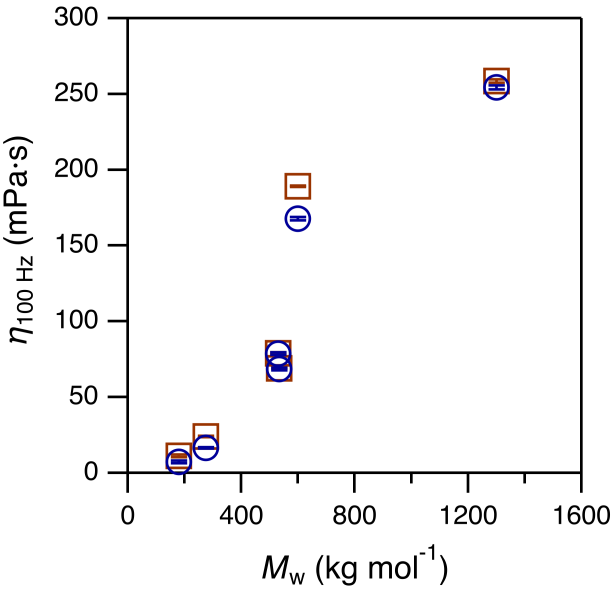

Figure 6 Viscosity of PVDF solutions for homopolymers of varying molecular weights, M_w, before (□) and after (○) centrifugation.

8 Stress–strain flow curves for cathode slurries

The stress–strain flow curves for cathode slurries comprising homopolymer and blends of PVDF are shown in Fig. 7.

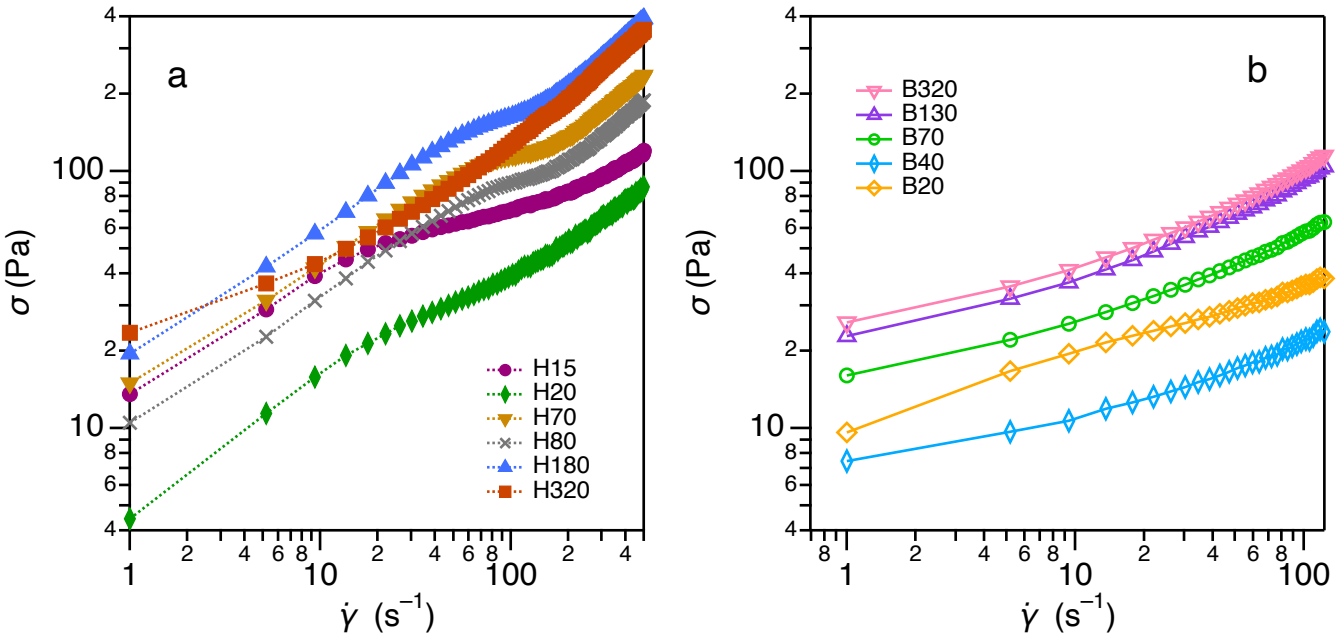

Figure 7 Stress–strain curves for cathode slurries comprising NMC811/CB/PDVF (90:5:5 w/w/w) with 41 wt% solids loading in NMP. a) Homopolymer PVDF and b) blends of PVDF. Samples are labelled 'H' for homopolymer or 'B' for blend alongside the viscosity of the PVDF solution in mPa·s. Lines are a guide for the eye.

9 Fitting the apparent yield stress of cathode slurries

Yield stresses, σ_0, were fitted to strain–stress curves following a method developed by Barnes[5]. A linear fit to the strain rate at high values of stress models hypothetical Newtonian behaviour (see Fig. 8a). The yield stress is given by the stress at which the Newtonian model diverges from the measured data. This value is inherently sensitive to the number of data points used to fit the Newtonian model. The fitting was automated to sample a broad range of potential starting points for the linear fit and the last point was always the highest strain rate measured. For each potential fit, the yield stress and R^2 value of the fit were recorded (see Fig. 8b). An arbitrary cutoff of $R^2 \geq 0.990$ was chosen, and all fits that met this criteria were accepted. The yield stresses corresponding to these 'accepted' fits were averaged to give a single value; error bars represent the standard deviation. The yield stresses thereby determined were not highly sensitive to the threshold value chosen. We are certain that the fitting did not artificially introduce a minimum into the data as the same trend is reflected in the raw viscosity data (see Fig. 1d).

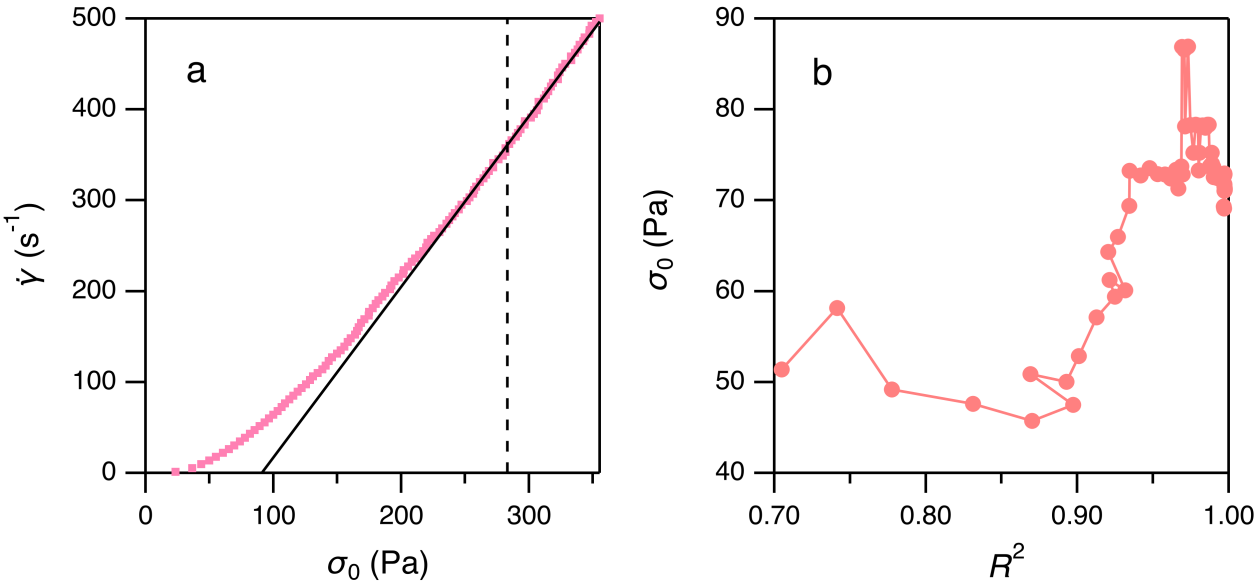

Figure 8 Determination of yield stress from rheological data. a) Strain rate vs stress for the NMC/CB/PVDF (90:5:5 w/w/w) cathode slurry comprising H320. The solid line is a linear fit to the high-stress data, the dashed line indicates the resulting yield stress. b) Yield stress, σ_0, vs the R^2 value for the linear fit for fits with a systematically decreasing number of data points.

10 Heat map of strain rates across gap heights and linear velocities

Comma bars, doctor blades and wire-bars are commonly used to coat battery cathodes on the laboratory scale; whereas slot dies are used commercially. The strain rate, $\dot{\gamma}$, applied to a coating relates to the linear velocity of the blade, v, and the thickness of the gap height between the substrate and the blade, h,

$$\dot{\gamma} = \frac{v}{h}.$$

The range of strain rates accessible using a particular draw down table is constrained by equipment practicalities (see Fig. 9), like chatter when the motor translates at a high velocity. A constant velocity of $\sim$6 mm s^{-1} was chosen to increase the uniformity of cathodes. At this velocity, the range of strain rates is 20–25 s^{-1}, far less than the strain rates required to significantly disrupt the carbon black structure in a cathode.

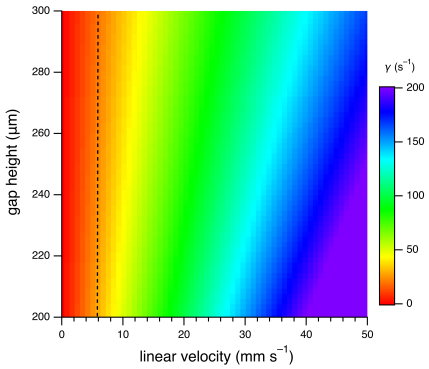

Figure 9 Heat map showing the strain rate, $\dot{\gamma}$, applied to a cathode slurry for the gap heights chosen for this work and the range of linear velocities accessible to the draw down table. The dotted line indicates a velocity of 5.8 mm s^{-1}, which was fixed for this work.

11 Krieger-Dougherty model of NMC dispersions

The viscosity of the freely-flowing NMC dispersions can be predicted using the Krieger–Dougherty relationship. In the high-shear limit, the measured viscosity of a slurry depends on the volume fraction of solid particles ϕ_s

$$\eta = \eta_\infty \left[1 - \frac{\phi_s}{\phi_m}\right]^{-[\eta]\phi_m} \tag{3}$$

where η_∞ is the viscosity of the unloaded polymer solution, ϕ_m is the maximum solids fraction at which flow can occur and $[\eta]$ is the intrinsic viscosity of the dispersion. For solid spheres in the high-shear limit $[\eta] = 2.5$. Values for ϕ_m vary between 0.495 and 0.605; here we choose $\phi_m = 0.605$ as the best approximation for a dispersion under high shear. Dispersions of NMC comprise $\phi_s = 0.25$, so the relative viscosity, $\eta_{rel} = \eta/\eta_\infty$, is predicted to be a constant value of 2.2. The measured values of relative viscosity are shown in Fig. 10. The relative viscosity of NMC dispersions varies between ~1 and 1.6, somewhat below the Krieger–Dougherty prediction of 2.2. Part of this disparity is likely due to the adsorption of PVDF onto NMC, which removes PVDF from solution, reducing the viscosity of the PVDF/NMP solution.

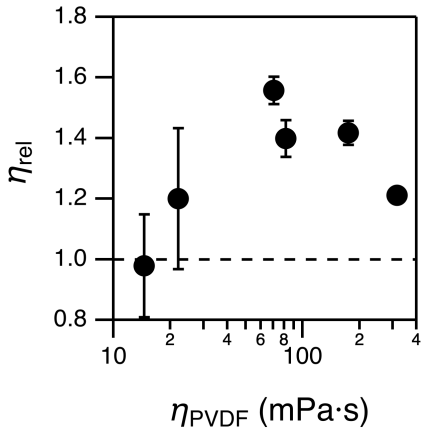

Figure 10 Relative viscosity of 41.8 wt% NMC dispersions in PVDF/NMP. The dashed line indicates that the viscosity of the NMC dispersion is identical to that of the PVDF/NMP solution.

12 Rheological properties of PVDF/NMP solutions and single-solid dispersions

The rheological properties of the homopolymer series of PVDF is studied across a range of partial slurries: solutions of PVDF in NMP, dispersions of NMC in PVDF solution and dispersions of CB in PVDF solutions. Decomposing the slurry in this way enables us to delineate the effect of each individual component upon the overall cathode slurry. The flow curves for each homopolymer and each partial slurry are shown in Fig. 11. Notably, the PVDF solutions and NMC dispersions are largely Newtonian across the range of shear rates studied. The CB dispersions are extremely shear-thinning with much higher viscosities than the NMC dispersions.

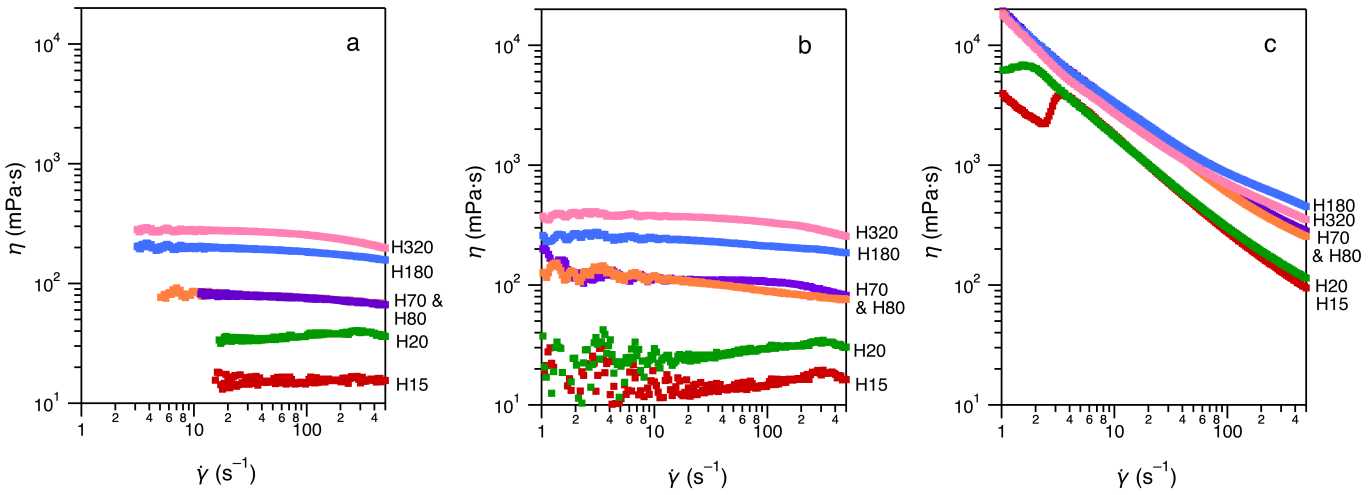

Figure 11 Rotational viscosity flow curves for a) PVDF/NMP solutions, b) 41.8 wt% NMC dispersions in PVDF/NMP and c) 3.8 wt% dispersions of CB in PVDF/NMP. In all cases the concentration of PVDF is 3.9 wt% in NMP. The initial viscosity of the PVDF/NMP solution is noted on each plot as Hxx, where 'H' denotes homopolymer PVDF and xx gives the viscosity of the solution in mPa·s.

The loss tangent was measured for the same samples (see Fig. 12). Only three of the polymer solutions could be measured, as the others flowed too easily for the oscillatory measurement. Only the dispersions made from these three PVDF samples are shown for clarity. The polymer solutions are all liquid-like at low frequencies and become more elastic at higher frequencies. The NMC dispersions exhibit similar behaviour to the polymer solutions; however, the CB dispersions are solid-like at all frequencies with a loss tangent that is almost independent of the frequency, which is the hallmark of a gel.

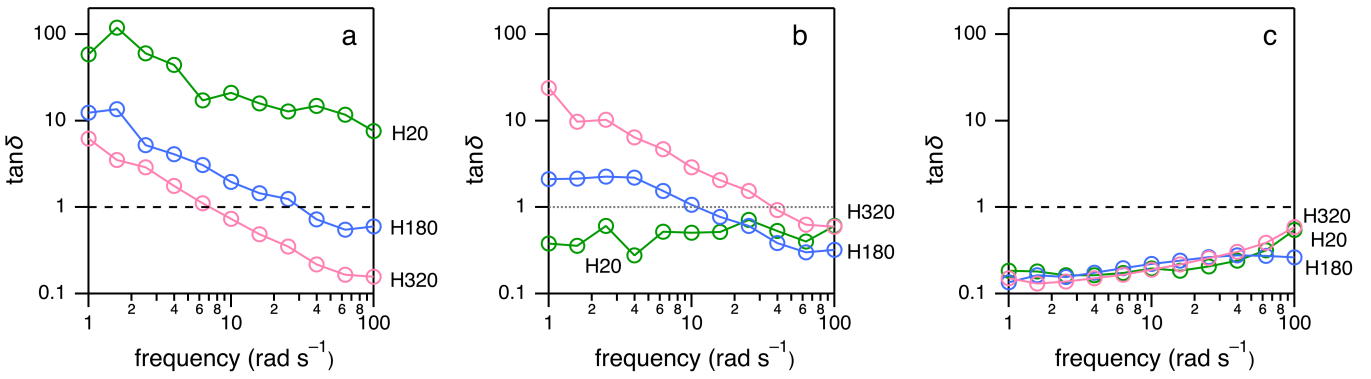

Figure 12 Loss tangent across a frequency sweep for a) PVDF/NMP solutions, b) 41.8 wt% NMC dispersions in PVDF/NMP and c) 3.8 wt% dispersions of CB in PVDF/NMP. In all cases the concentration of PVDF is 3.9 wt% in NMP. The initial viscosity of the PVDF/NMP solution is noted on each plot as Hxx, where 'H' denotes homopolymer PVDF and xx gives the viscosity of the solution in mPa·s.

The storage and loss moduli are measured for each PVDF homopolymer and partial slurry.

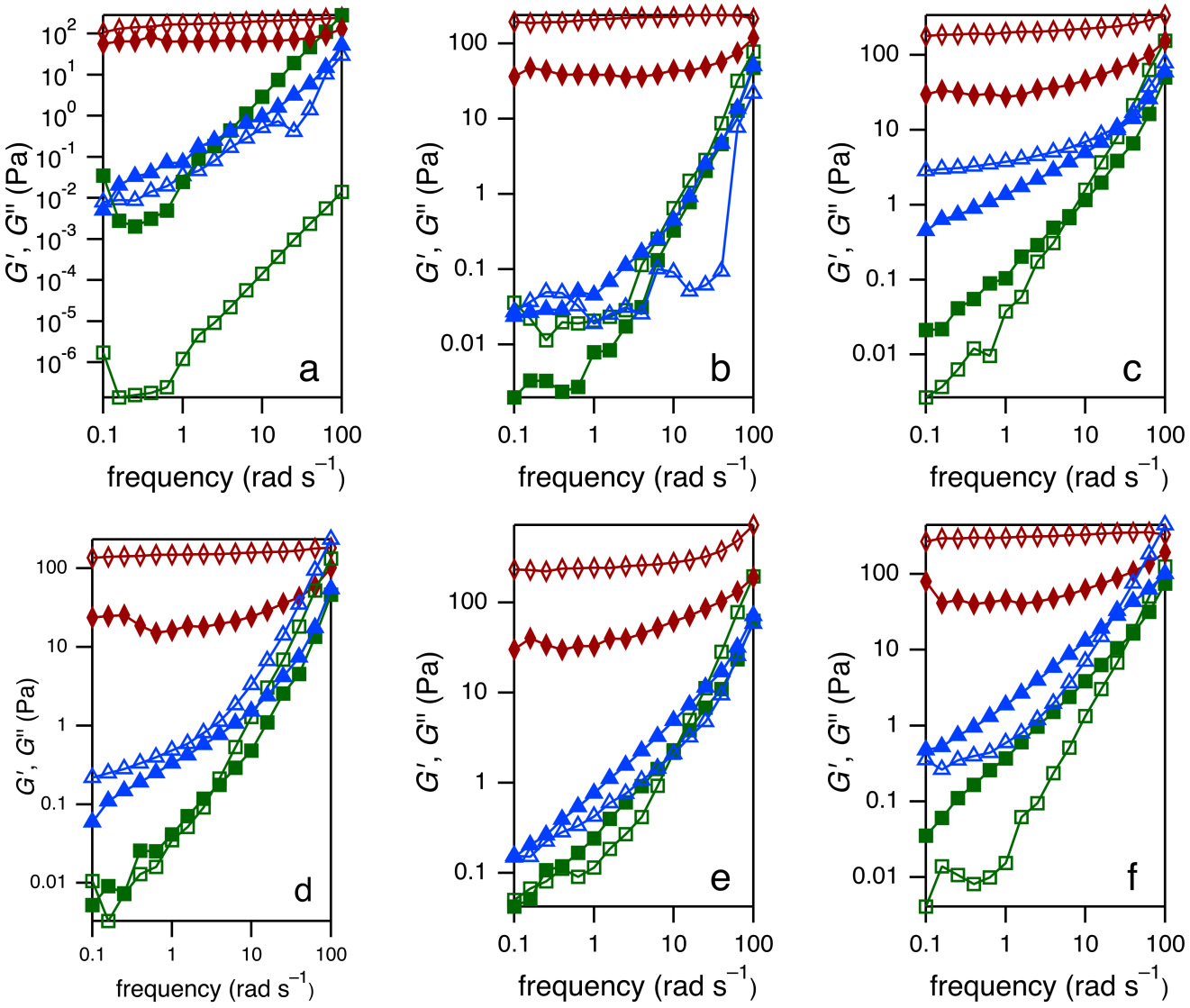

Figure 13 Storage and loss moduli for slurries comprising NMC/PVDF/NMP (41.8/2.3/55.9 wt%)G'(□), G''(■); slurries comprising CB/PVDF/NMP (3.8/3.8/92.3 wt%) G' (◊), G''(♦) and slurries comprising NMC/CB/PVDF/NMP (40.8/2.3/2.3/54.6 wt%) G' (△) and G'' (▲) for PVDF molecular weights a) 180 kg mol^{-1} b) 275 kg mol^{-1} c) 530 kg mol^{-1} d) 534 kg mol^{-1} e) 600 kg mol^{-1} and f) 1,300 kg mol^{-1}.

13 Areal adsorption of PVDF onto solid particles

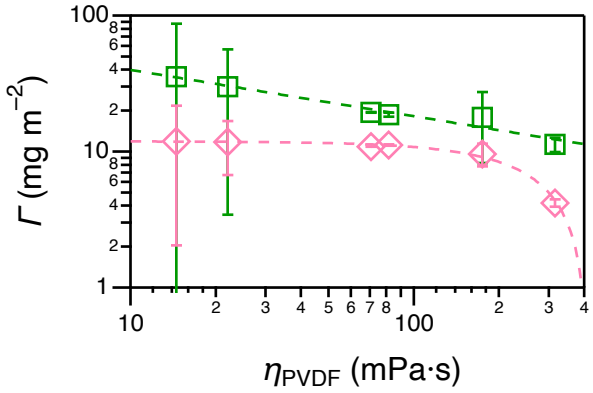

Figure 14 Areal adsorption (mass of adsorbed binder per surface area of solid) of PVDF binder onto CB and NMC solids. Dashed lines are power law fits to the data.

14 Particle size distribution of CB as a function of dispersion age

The particle size distribution of CB was measured for dispersions of CB in PVDF solution (see Fig. 15a). Measurements were made immediately after mixing and diluting the dispersion, the samples were aged without agitation for 4 days, and the measurements were repeated. In all cases, the mean particle size decreases with time. There is mechanism for deagglomeration of the CB during ageing, so the average particle size must decrease because larger particles in the sample settle under gravity. It is possible that particles could continue to flocculate during ageing, but the low concentration of CB (∼0.01 wt%) reduces the probability of particle collisions. Whilst the change in mean particle size with ageing is modest for the high-viscosity samples, there is a 50%–100% difference for the samples with either no PVDF or the lowest viscosity PVDF. These two samples were measured first in the series, and each measurement took ∼ 20 min. It is possible that there is less of an ageing effect in other samples in the series because the largest particles had already settled prior to the first measurement.

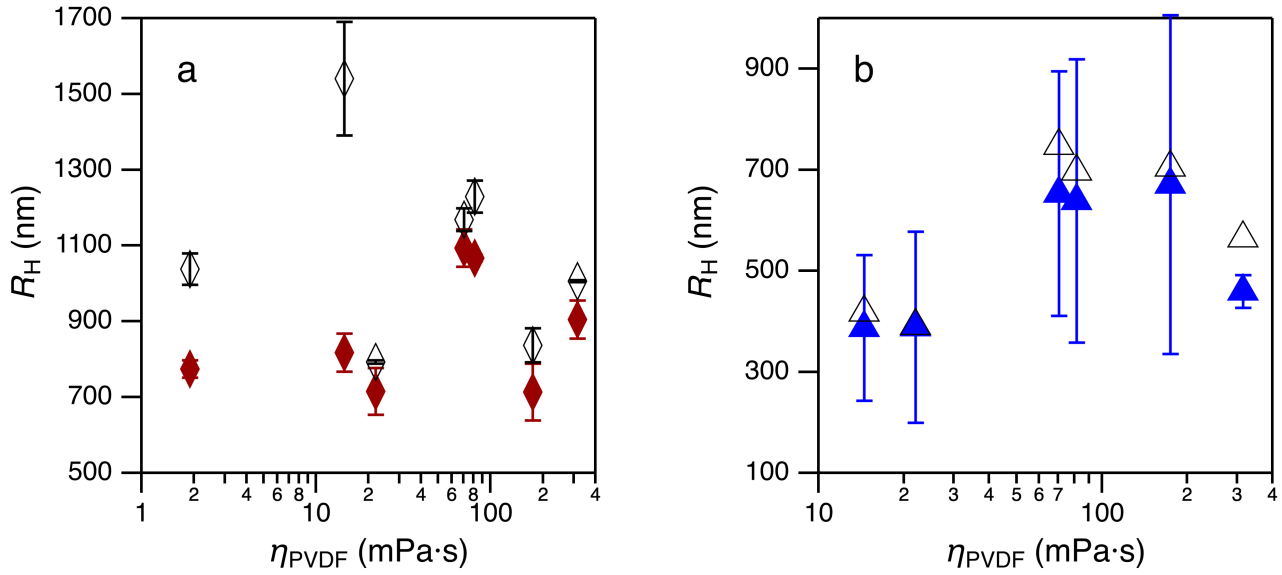

Figure 15 Volume-averaged hydrodynamic radius, R_H, of CB particles in diluted dispersions comprising a) CB/PVDF/NMP 1:1:24 wt% measured immediately after mixing (◊) and aged 4 days (♦) and b) NMC/CB/PVDF (90:5:5 w/w/w) dispersed in NMP at a solids loading of 40.8 wt% and aged 24 h (△) and 40 h (▲). Error bars indicate the width of the distribution of particle sizes.

In order to validate an appropriate time in the ageing process for reproducible measurements, diluted cathode slurries were measured 24 and 40 h after mixing and dilution (see Fig. 15b). Again, the most aged samples exhibit a smaller mean radius of CB than the less aged samples. The two time measurements are relatively close together for each sample and there is no change in the trend between samples. As a result, a settling period of 24 h was accepted for the standard procedure.

15 Dry electrode thicknesses

Table 3 Dry film thicknesses of the cathodes imaged using SEM

sample name	PVDF M_w (kg mol^{-1})	Electrode film thickness (μm)
H15	180	82.67 ± 2.05
H20	275	83.00 ± 2.16
H70	530	88.00 ± 1.87
H80	534	88.25 ± 2.77
H180	600	88.50 ± 1.80
H320	1,300	89.25 ± 1.09

16 Scanning electron micrographs of the cathode surface peeled from the current collector

Cathode films were manually peeled off their current collectors in order to access the interface that was in contact with the current collector. SEM images of these interfaces are shown in Fig. 16.

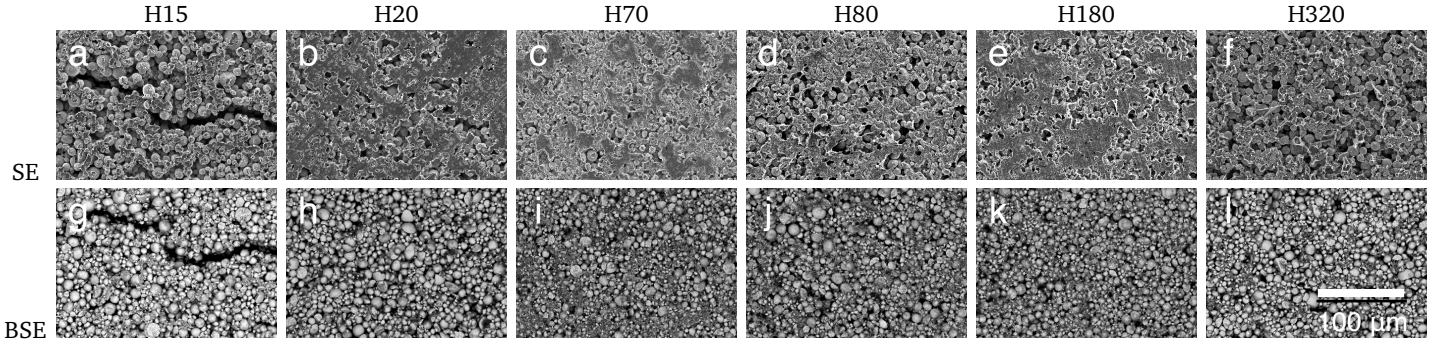

Figure 16 Scanning electron micrographs for NMC/CB/PVDF (90/5/5 wt%) films formed using 3.9 wt% PVDF/NMP solutions with varying viscosity achieved by changing the molecular weight of the PVDF. The films were peeled off the current collector to image the interface in contact with foil. Secondary electron (SE) and backscattering (BSE) micrographs, respectively are shown for samples: H15 (180 kg mol^{-1}) a) and g); H20 (275 kg mol^{-1}) b) and h); H70 (530 kg mol^{-1}) c) and i); H80 (534 kg mol^{-1}) d) and j); H180 (600 kg mol^{-1}) e) and k); and H320 (1,300 kg mol^{-1}) f) and l). The scale bar shown in l) indicates 100 µm and applies to all images.

17 Sedimentation of NMC cathode particles in slurries

The settling velocity of solid particles in a slurry is given by

$$u_s = \frac{g d_p^2 (\rho_s - \rho_l)}{18 \eta_0} (1 - \phi_s)^m \tag{4}$$

where g is the gravitational constant, $g = 9.81$ m s^{-2}; d_p is the diameter of the particle, taken as the volume-averaged particle diameter measured from particle sizing, $d_p = 12.8$ μm; ρ_s is the density of the solid particle, ρ_l is the density of the solution, η_0 is the zero-shear viscosity of the solution, $\phi_s = 0.241$ is the volume fraction of NMC solid particles and m is an empirical parameter that depends upon the Reynold's number describing Stoke's flow around the particle. The tap density of Targray NMC811 is $\rho_{\text{tap}} = 2,310$ kg m^{-3} as reported by the manufacturer[6]. Assuming a volumetric particle packing density of 60%, the density of an average particle would be $\rho_s = 3,850$ kg m^{-3}. The density of NMP at 25°C is $\rho_{\text{NMP}} = 1.028$ kg m^{-3} according to the manufacturer[7]. Assuming zero excess volume of mixing for PVDF/NMP solutions at 3.9 wt% PVDF, the solution density is $\rho_l = 1,069$ kg m^{-3}. The Reynold's number for flow around a falling particle is given by

$$Re = \frac{\rho_l u_s d_p}{\eta_0}. \tag{5}$$

For Re < 0.2, the exponent in Eqn. 4 is given by $m = 4.65$[8]. The Newtonian region of the viscosity flow curves is used to determine η_0 for each PVDF/NMP solution. The settling velocity and Reynold's number are given for each PVDF/NMP solution in Table 4. All of the calculated Reynold's numbers are much less than 0.2, validating the value chosen for m.

Table 4 Fitted and calculated values related to the settling velocity of NMC in 3.9 wt% PVDF solutions

PVDF/NMP sample	η_0 (mPa·s)	u_s (nm s^{-1})	Re $\times 10^7$
H15	14.5	4,750	44.8
H20	22.0	3,130	29.5
H70	70.6	978	9.22
H80	81.4	848	7.99
H180	175	395	3.73
H320	316	219	2.06

Notably, the settling velocities are expected to underestimate the initial settling velocity of particles, as the viscosity of the solutions was measured at 25°C, but the films are dried under 80°C air.

18 Physical properties of cathodes

The mass of each cathode, m_{cat}, was measured by weighing the dry cathode and subtracting the fixed mass of the current collector. The thickness of each cathode was measured using a micrometer at various locations on the cathode, averaging the results and subtracting the fixed thickness of the current collector. All cathodes were 12-mm in diameter, areal mass loading, m_{areal}, was calculated as

$$m_{\text{areal}}\,\frac{\text{g}}{\text{m}^2} = \frac{m_{\text{cat}}\ \text{mg} \times \frac{1\ \text{g}}{1000\ \text{mg}}}{\pi \times \left(12\ \text{mm} \times \frac{1\ \text{m}}{1000\ \text{mm}}\right)^2}.$$

Table 5 Measured and calculated physical properties of NMC811/CB/PVDF (95:5:5 w/w/w) cathodes formulated from PVDF homopolymer solutions of differing viscosity. 'Hxxy' denotes the homopolymer PVDF solution with viscosity xx in mPa·s and y is the replicate indicator.

sample reference	m_{areal} (g m^{-2})	thickness (μm)
H15a	48.3	48.2
H15b	159.7	152.2
H15c	198.1	165.2
H20b	88.0	65.2
H20c	85.7	75.2
H70a	125.2	85.2
H70b	125.2	130.2
H70c	121.4	79.2
H80a	141.2	80.2
H80b	127.3	85.2
H80c	152.3	113.2
H180a	129.0	82.2
H180b	123.0	84.2
H180c	130.6	81.2
H320a	118.4	68.2
H320b	136.2	76.2
H320c	134.3	72.2
H320d	122.7	66.2

19 Capacity fade for replicate cells

At least three replicates of each battery half-cell were cycled, but in some cases, the replicates failed to cycle at 1C or the data were extremely noisy. The thickness and areal mass loading of each replicate is reported in Table 5

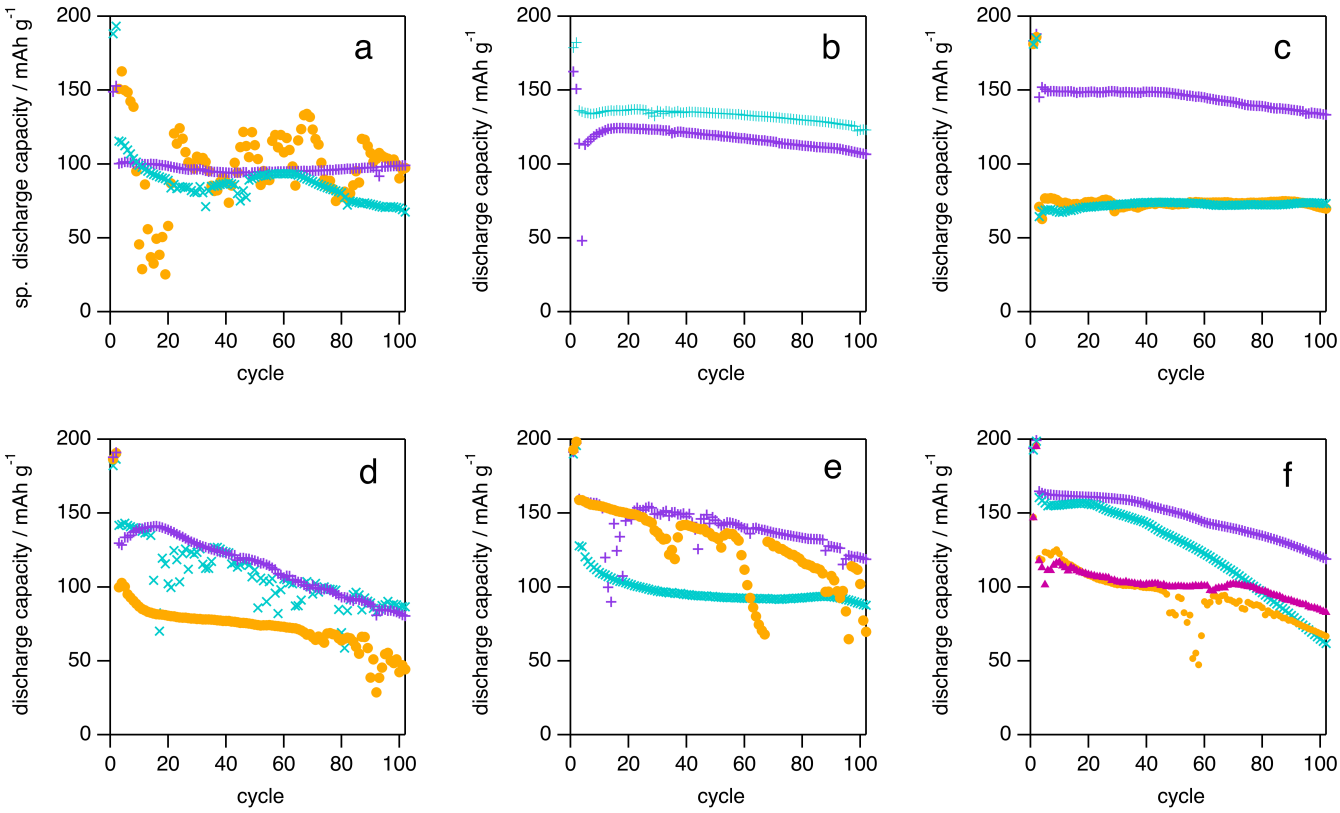

Figure 17 Specific discharge capacity during cycling for individual battery half cells comprising NMC811:CB:PVDF (90:5:5 w/w/w) with different initial viscosities for the PVDF/NMP solutions: a) H15, b) H20, c) H70, d) H80, e) H180, f) H320 where Hxx denotes a homopolymer solution with viscosity xx in mPa·s. Markers are used for sample replicates a(+), b(×), c(●) and d(▲). The first two cycles are carried out at C/20 to form the solid–electrolyte interface and the subsequent 100 cycles (cycles 3 to 102) are carried out at 1C.

20 Electrochemical performance of each cell

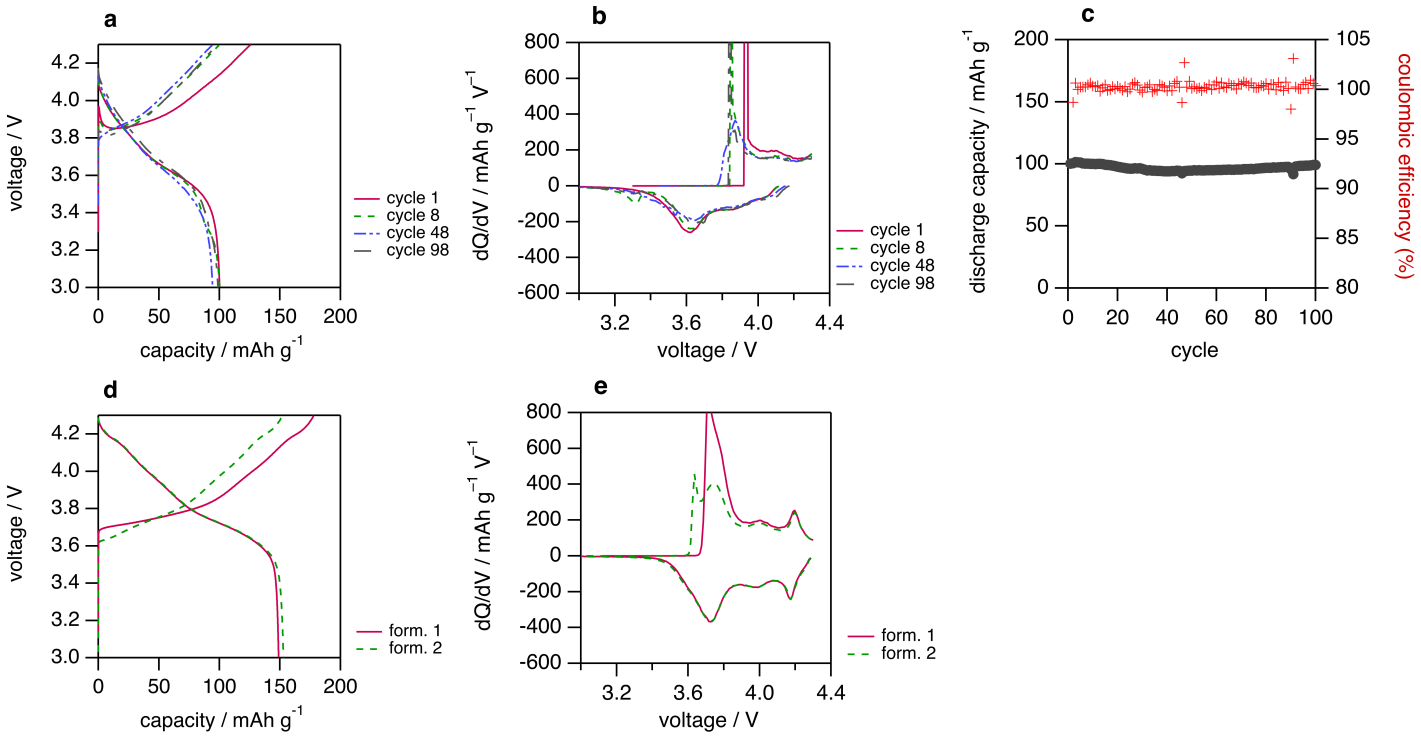

Figure 18 Electrochemical performance for cell H15a (see Table 5 for composition. a) Charge and discharge curves and b) dQ/dV curves for selected cycles at 1C. c) Capacity fade over 100 cycles. d) Charge and discharge curves and e) dQ/dV curves for the two formation cycles at C/20.

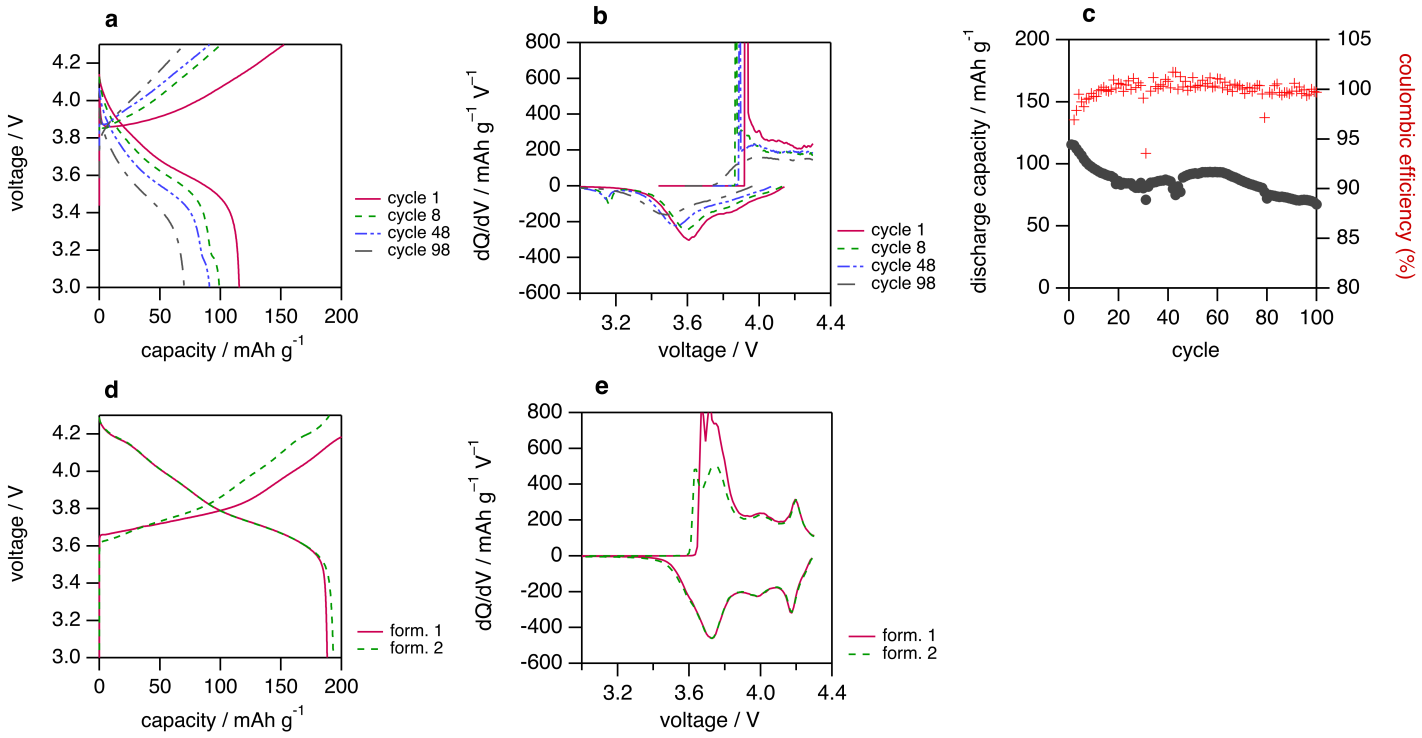

Figure 19 Electrochemical performance for cell H15b (see Table 5 for composition. a) Charge and discharge curves and b) dQ/dV curves for selected cycles at 1C. c) Capacity fade over 100 cycles. d) Charge and discharge curves and e) dQ/dV curves for the two formation cycles at C/20.

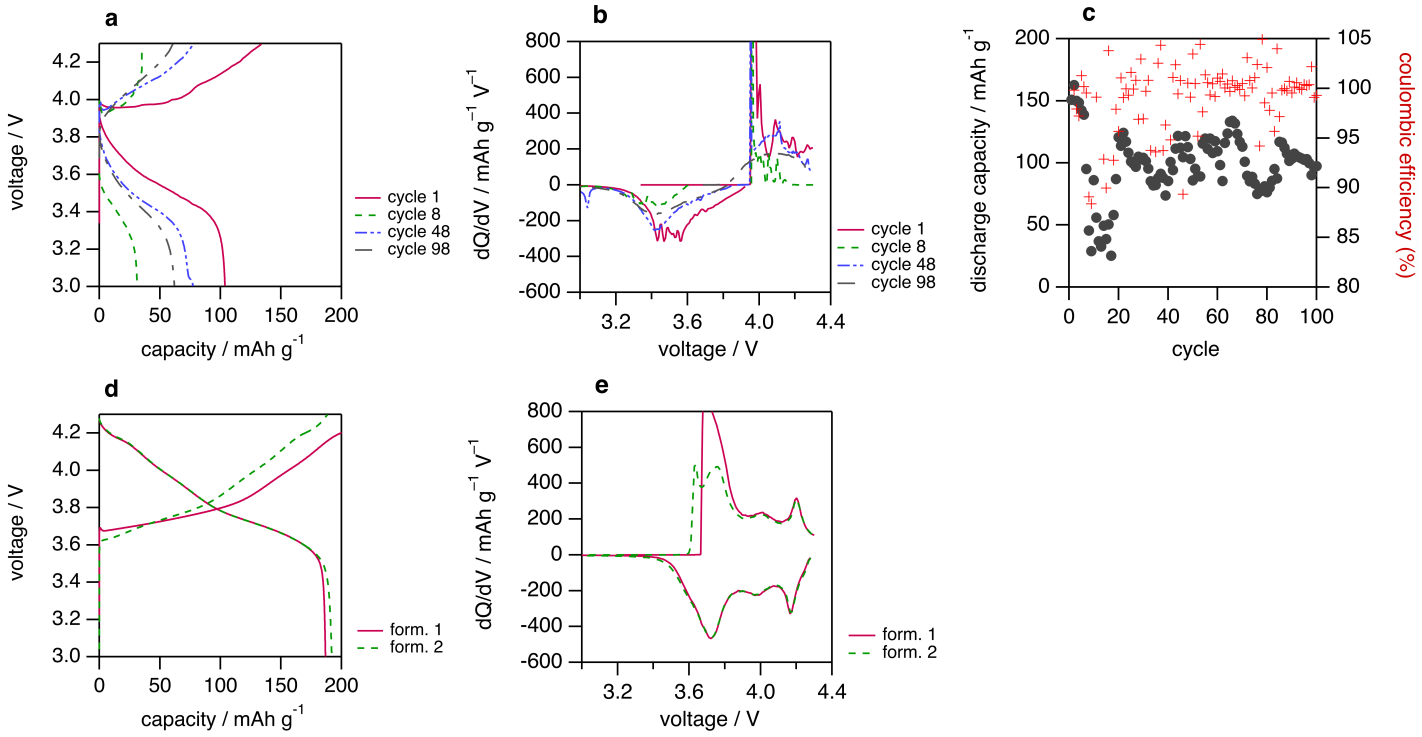

Figure 20 Electrochemical performance for cell H15c (see Table 5 for composition. a) Charge and discharge curves and b) dQ/dV curves for selected cycles at 1C. c) Capacity fade over 100 cycles. d) Charge and discharge curves and e) dQ/dV curves for the two formation cycles at C/20.

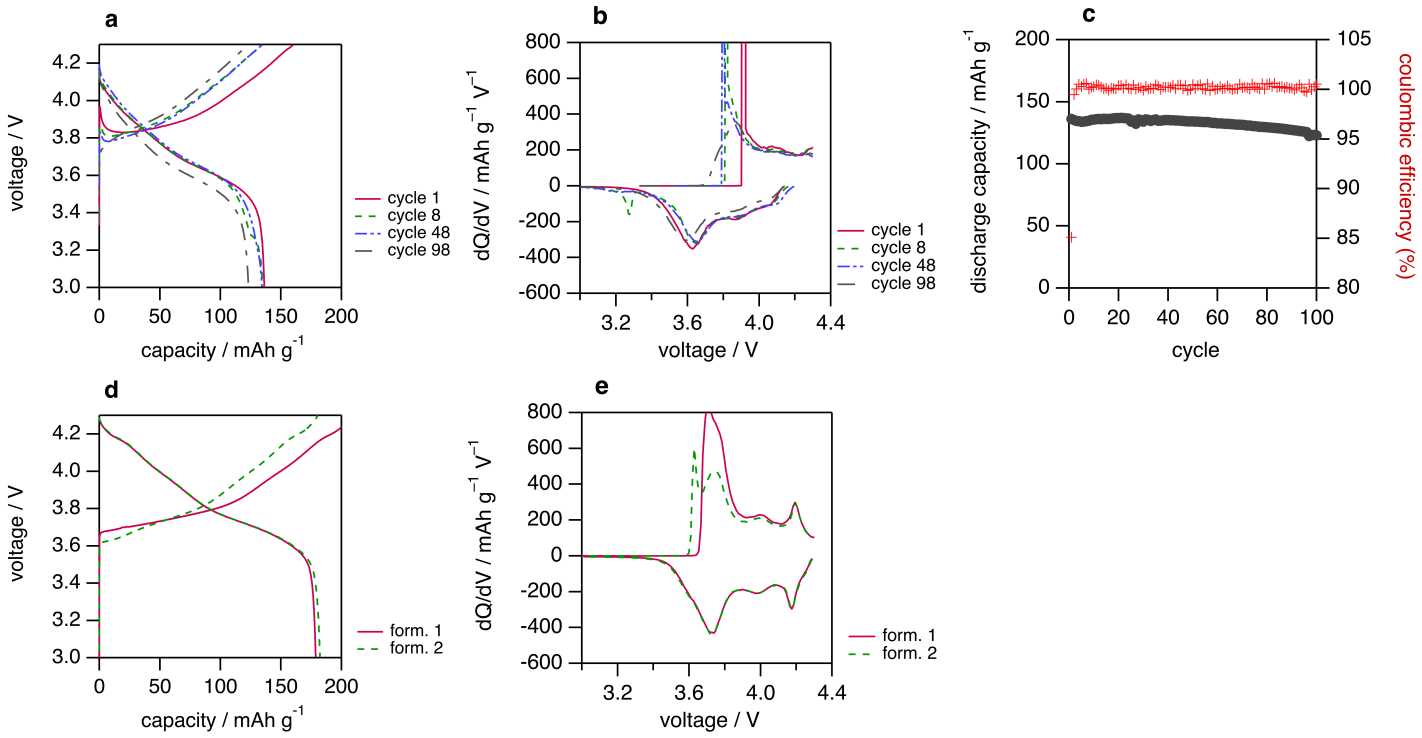

Figure 21 Electrochemical performance for cell H20b (see Table 5 for composition. a) Charge and discharge curves and b) dQ/dV curves for selected cycles at 1C. c) Capacity fade over 100 cycles. d) Charge and discharge curves and e) dQ/dV curves for the two formation cycles at C/20.

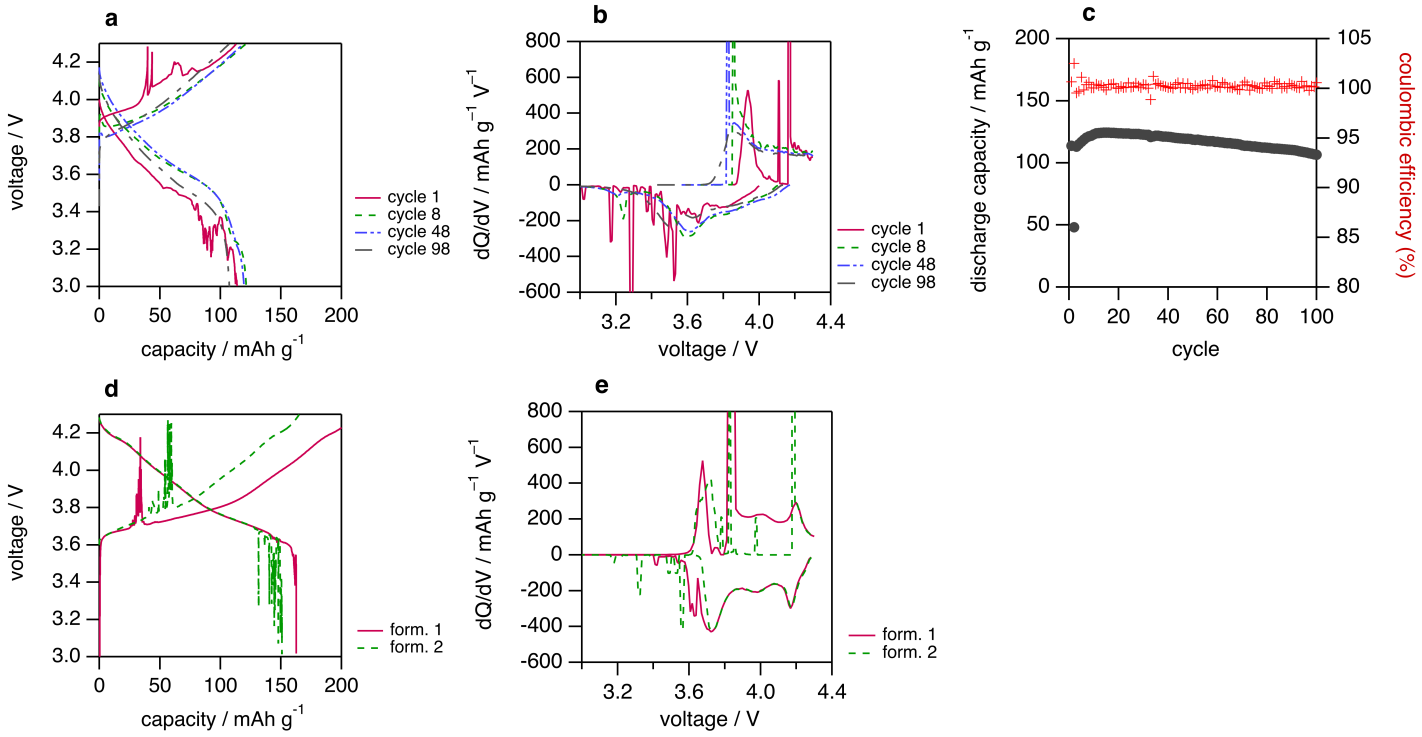

Figure 22 Electrochemical performance for cell H20c (see Table 5 for composition. a) Charge and discharge curves and b) dQ/dV curves for selected cycles at 1C. c) Capacity fade over 100 cycles. d) Charge and discharge curves and e) dQ/dV curves for the two formation cycles at C/20.

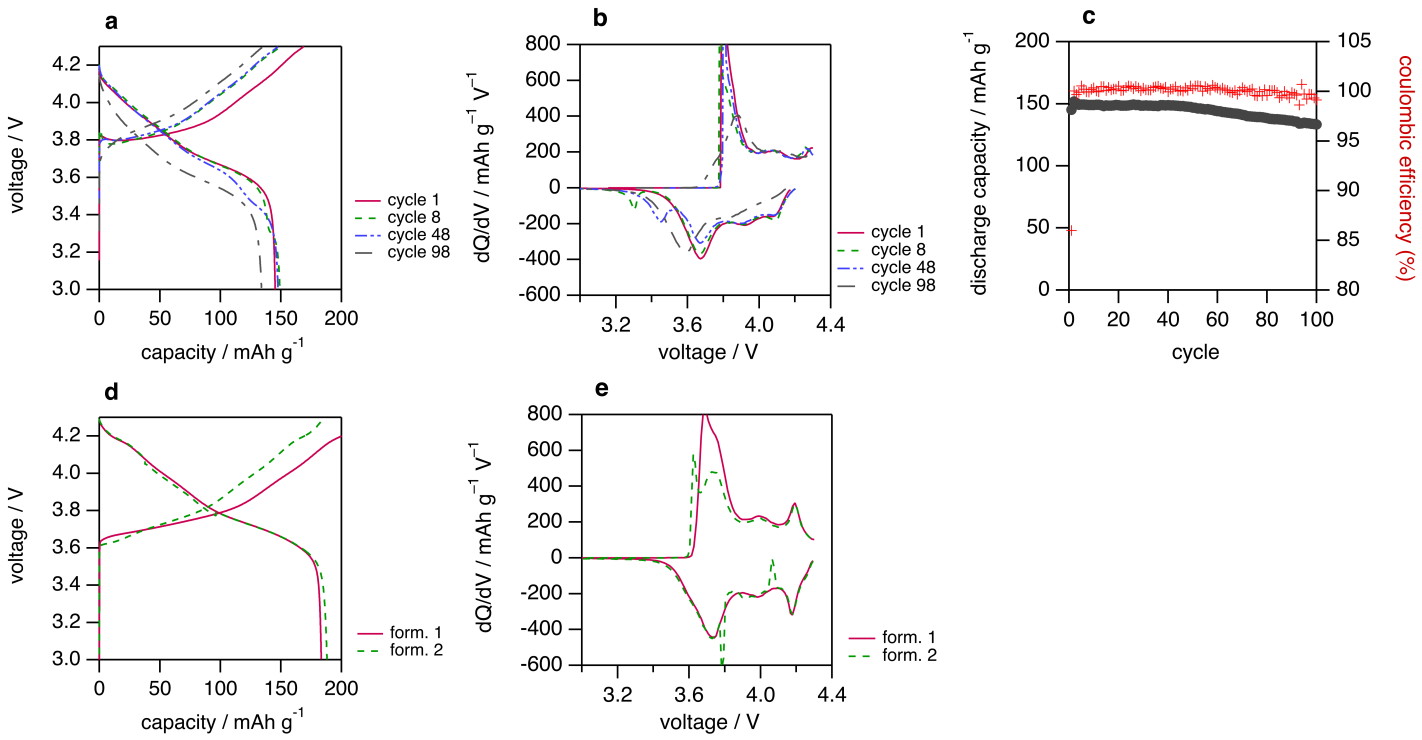

Figure 23 Electrochemical performance for cell H70a (see Table 5 for composition. a) Charge and discharge curves and b) dQ/dV curves for selected cycles at 1C. c) Capacity fade over 100 cycles. d) Charge and discharge curves and e) dQ/dV curves for the two formation cycles at C/20.

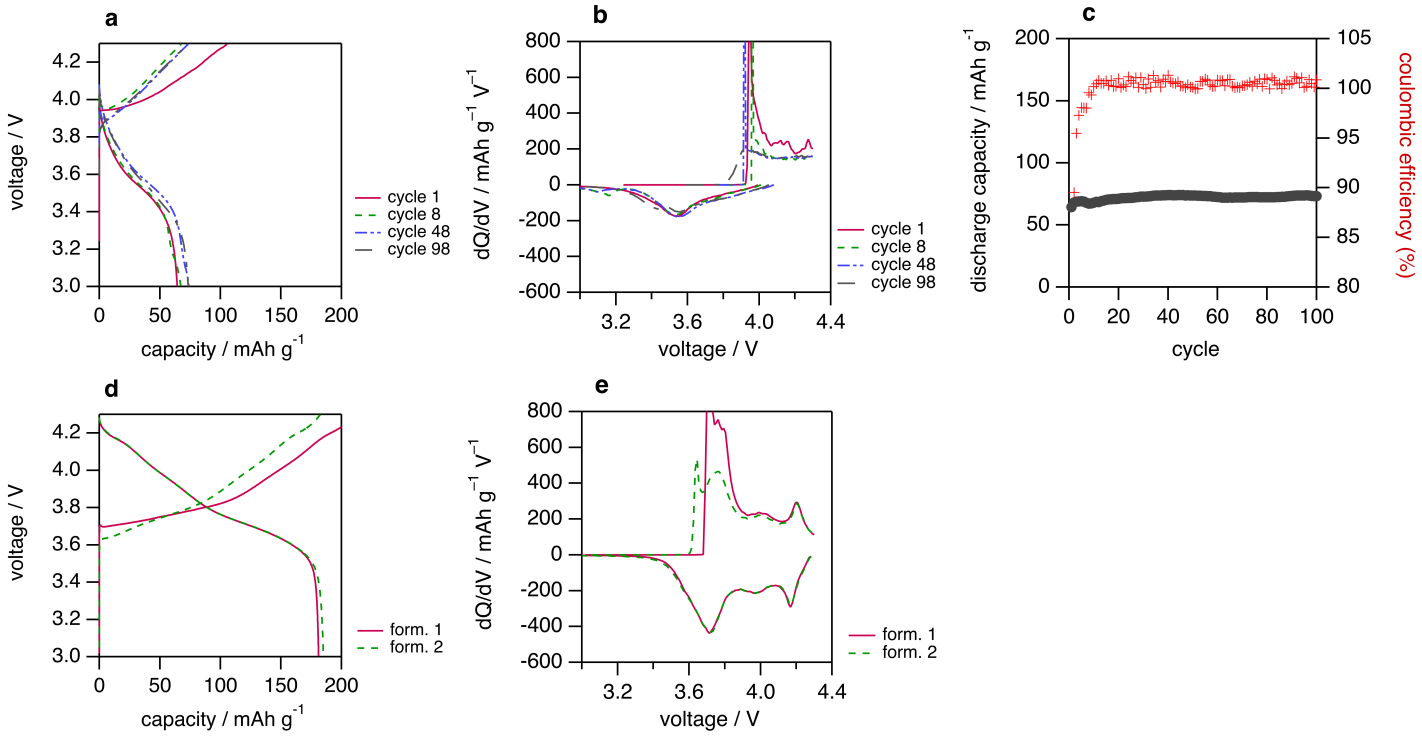

Figure 24 Electrochemical performance for cell H70b (see Table 5 for composition. a) Charge and discharge curves and b) dQ/dV curves for selected cycles at 1C. c) Capacity fade over 100 cycles. d) Charge and discharge curves and e) dQ/dV curves for the two formation cycles at C/20.

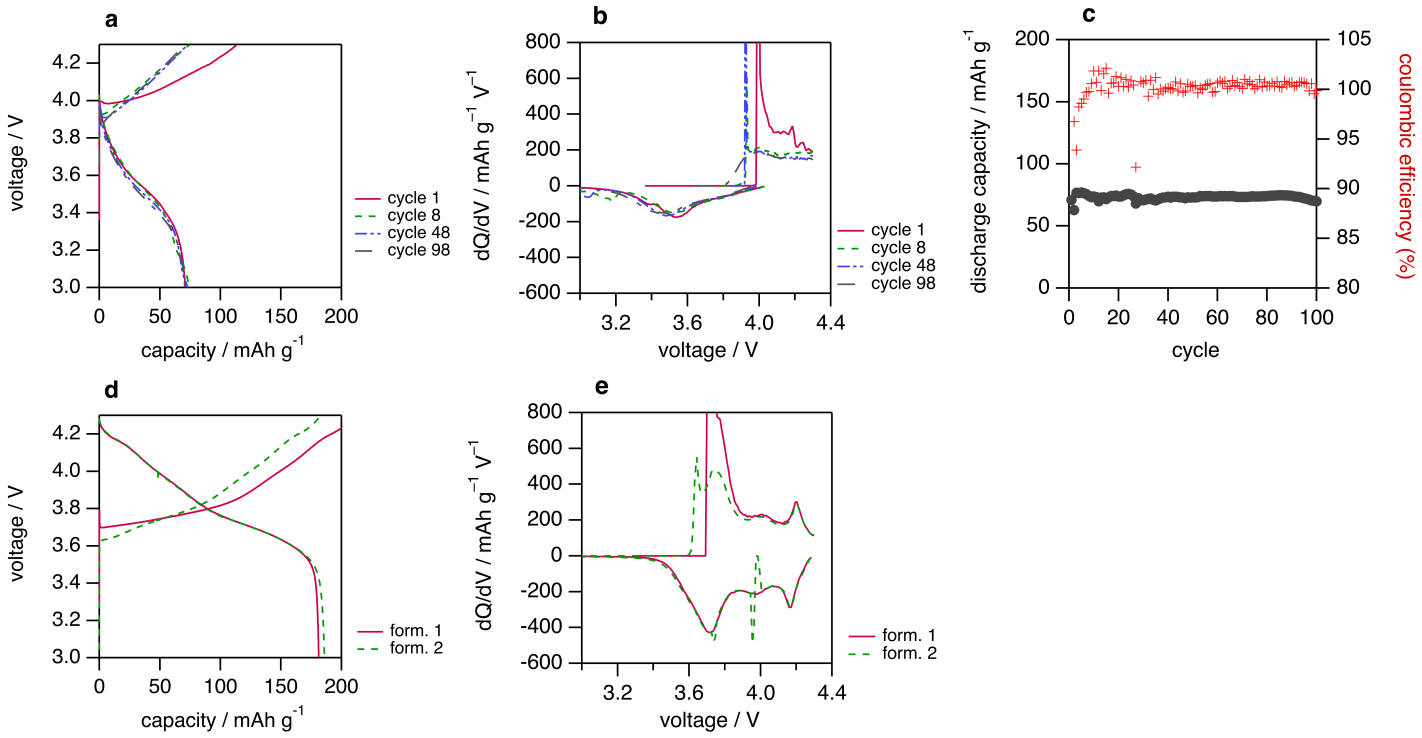

Figure 25 Electrochemical performance for cell H70c (see Table 5 for composition. a) Charge and discharge curves and b) dQ/dV curves for selected cycles at 1C. c) Capacity fade over 100 cycles. d) Charge and discharge curves and e) dQ/dV curves for the two formation cycles at C/20.

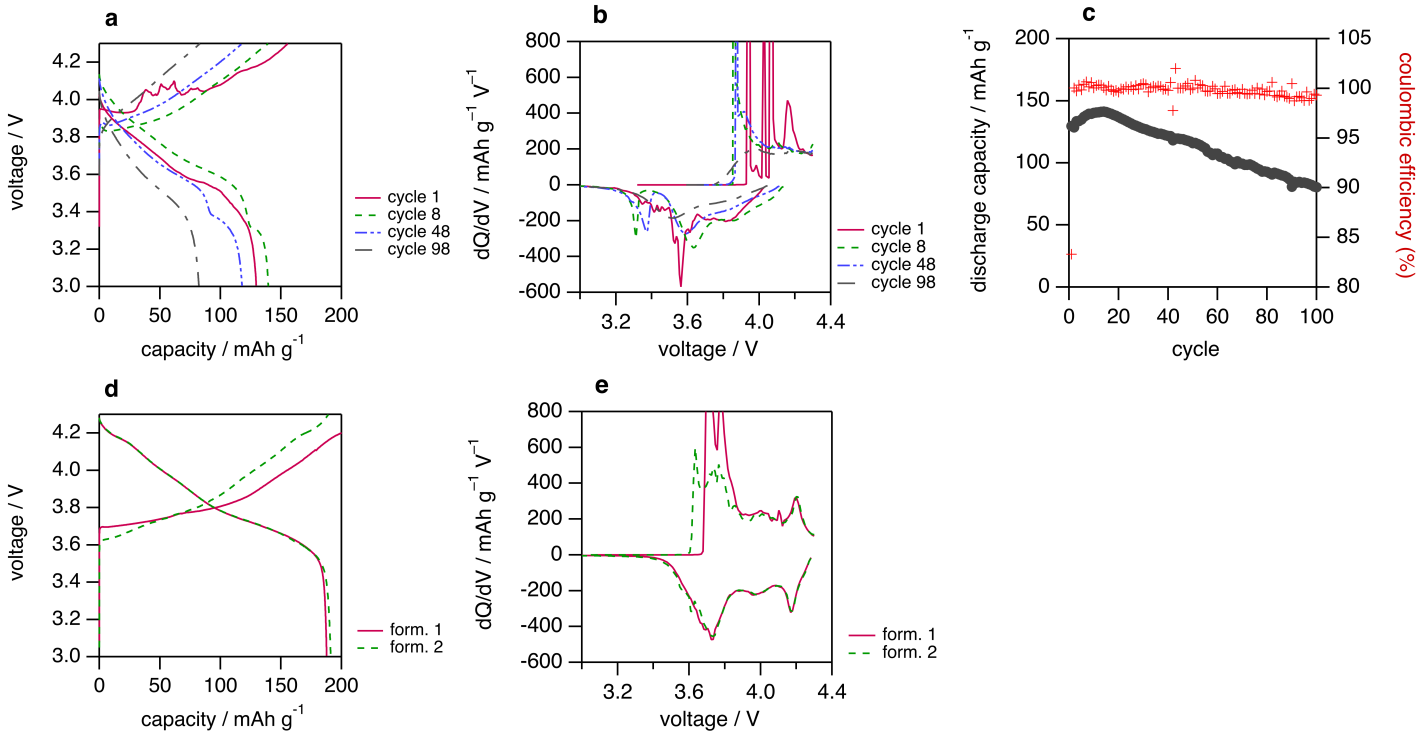

Figure 26 Electrochemical performance for cell H80a (see Table 5 for composition. a) Charge and discharge curves and b) dQ/dV curves for selected cycles at 1C. c) Capacity fade over 100 cycles. d) Charge and discharge curves and e) dQ/dV curves for the two formation cycles at C/20.

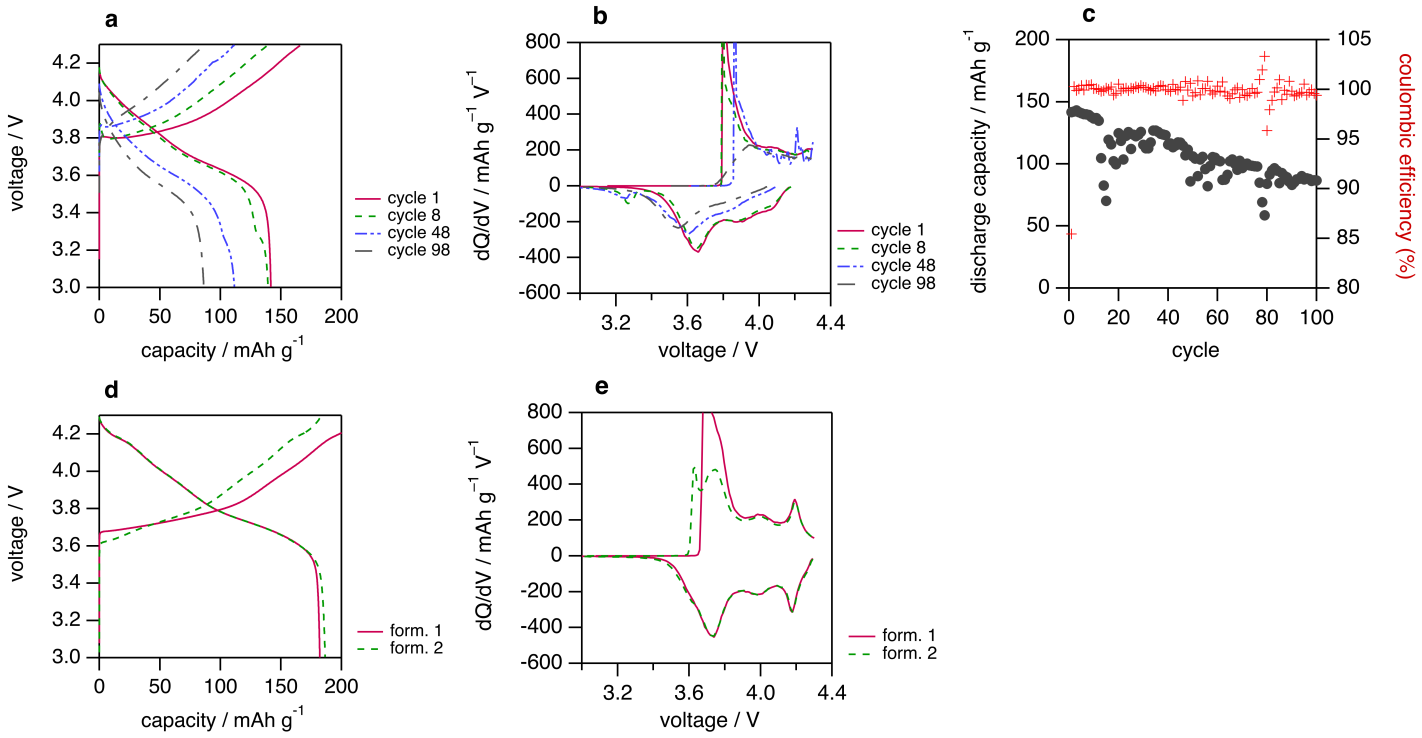

Figure 27 Electrochemical performance for cell H80b (see Table 5 for composition. a) Charge and discharge curves and b) dQ/dV curves for selected cycles at 1C. c) Capacity fade over 100 cycles. d) Charge and discharge curves and e) dQ/dV curves for the two formation cycles at C/20.

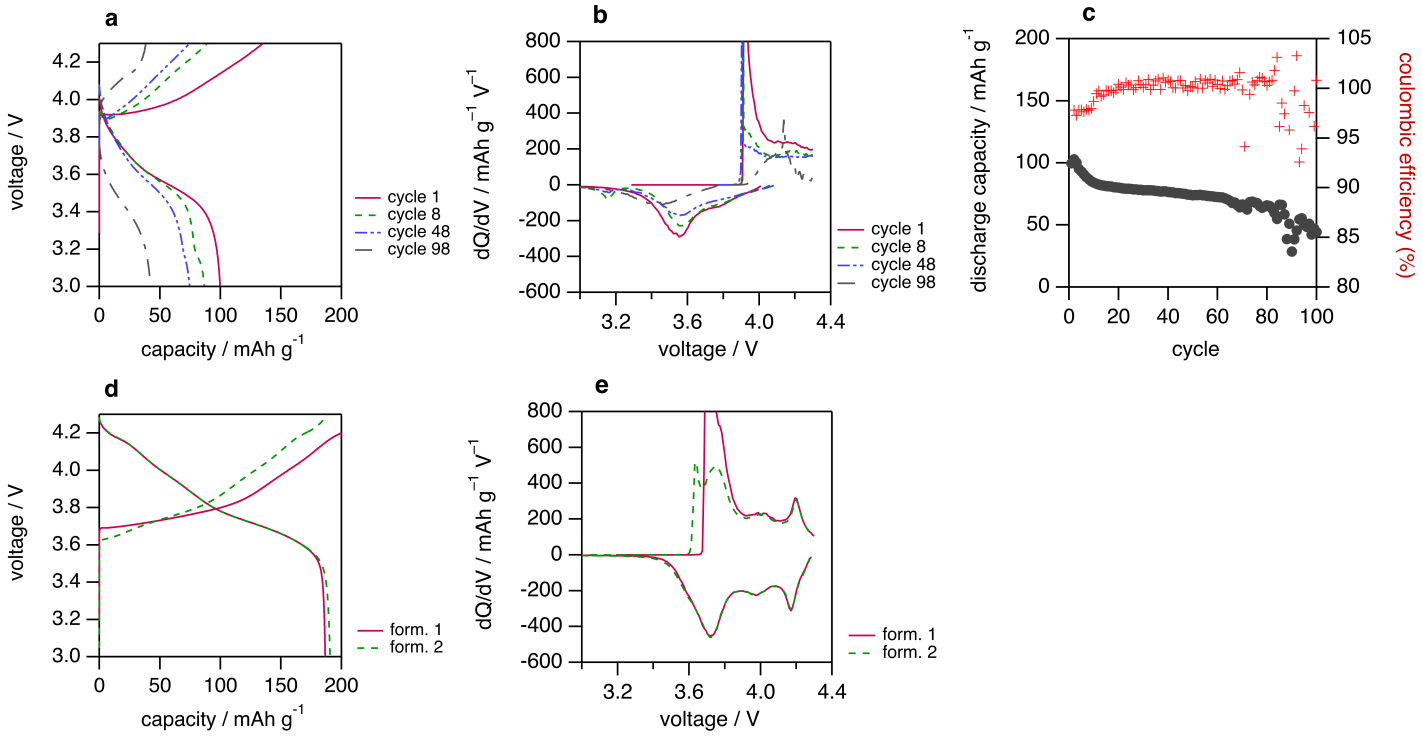

Figure 28 Electrochemical performance for cell H80c (see Table 5 for composition. a) Charge and discharge curves and b) dQ/dV curves for selected cycles at 1C. c) Capacity fade over 100 cycles. d) Charge and discharge curves and e) dQ/dV curves for the two formation cycles at C/20.

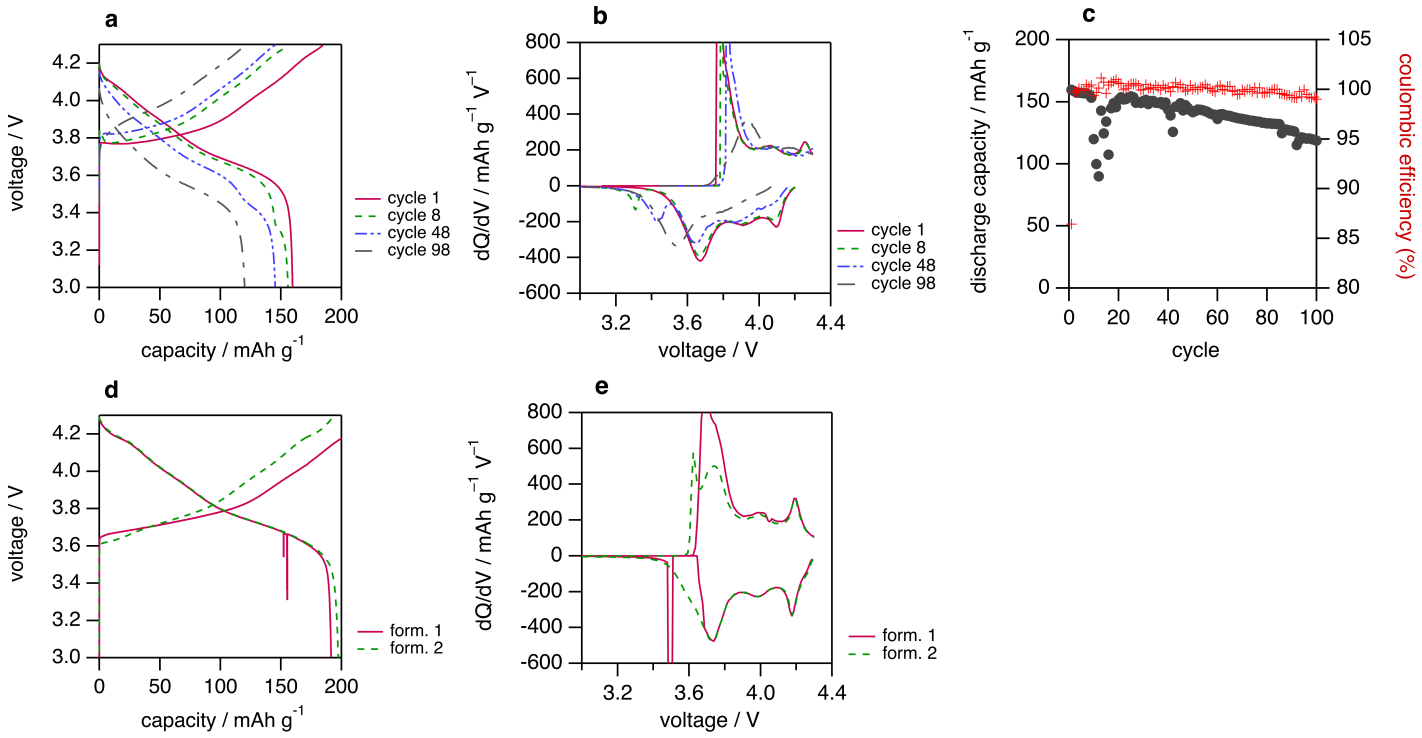

Figure 29 Electrochemical performance for cell H180a (see Table 5 for composition. a) Charge and discharge curves and b) dQ/dV curves for selected cycles at 1C. c) Capacity fade over 100 cycles. d) Charge and discharge curves and e) dQ/dV curves for the two formation cycles at C/20.

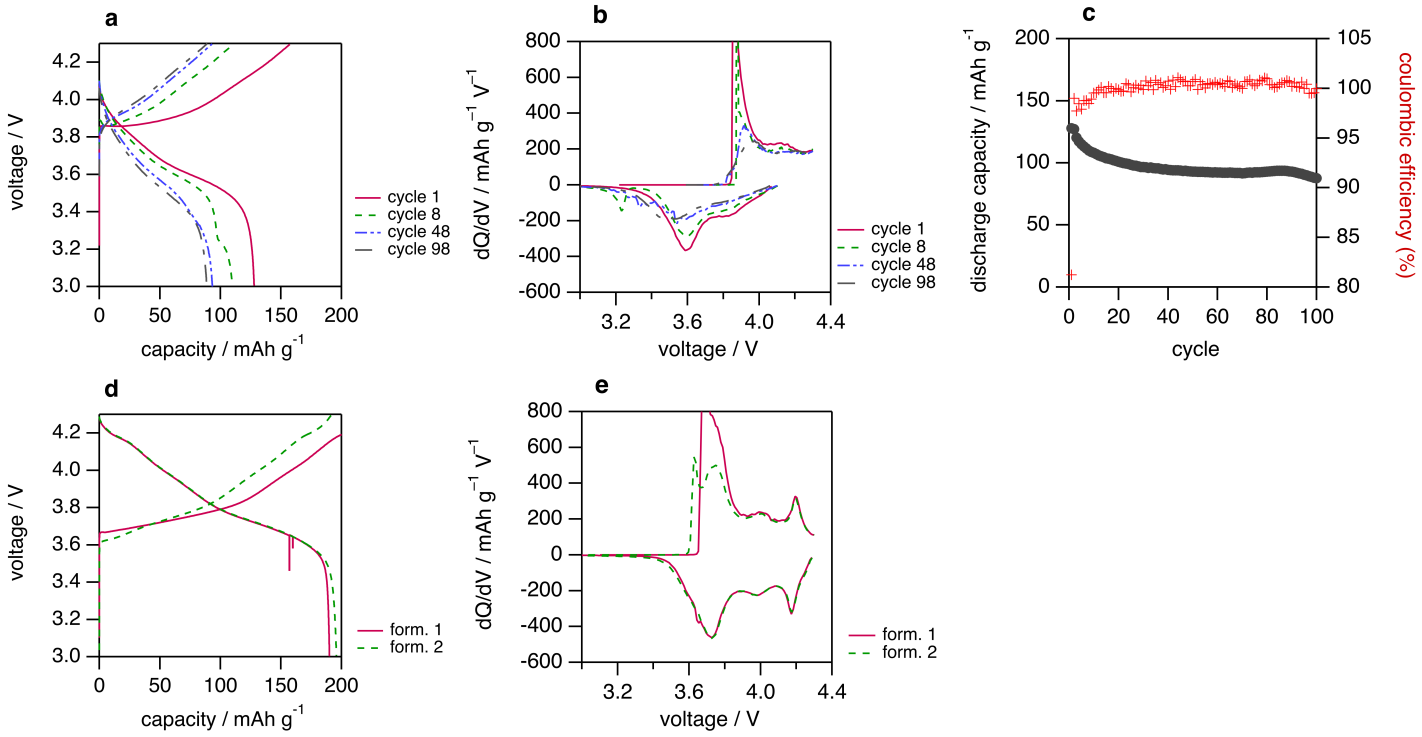

Figure 30 Electrochemical performance for cell H180b (see Table 5 for composition. a) Charge and discharge curves and b) dQ/dV curves for selected cycles at 1C. c) Capacity fade over 100 cycles. d) Charge and discharge curves and e) dQ/dV curves for the two formation cycles at C/20.

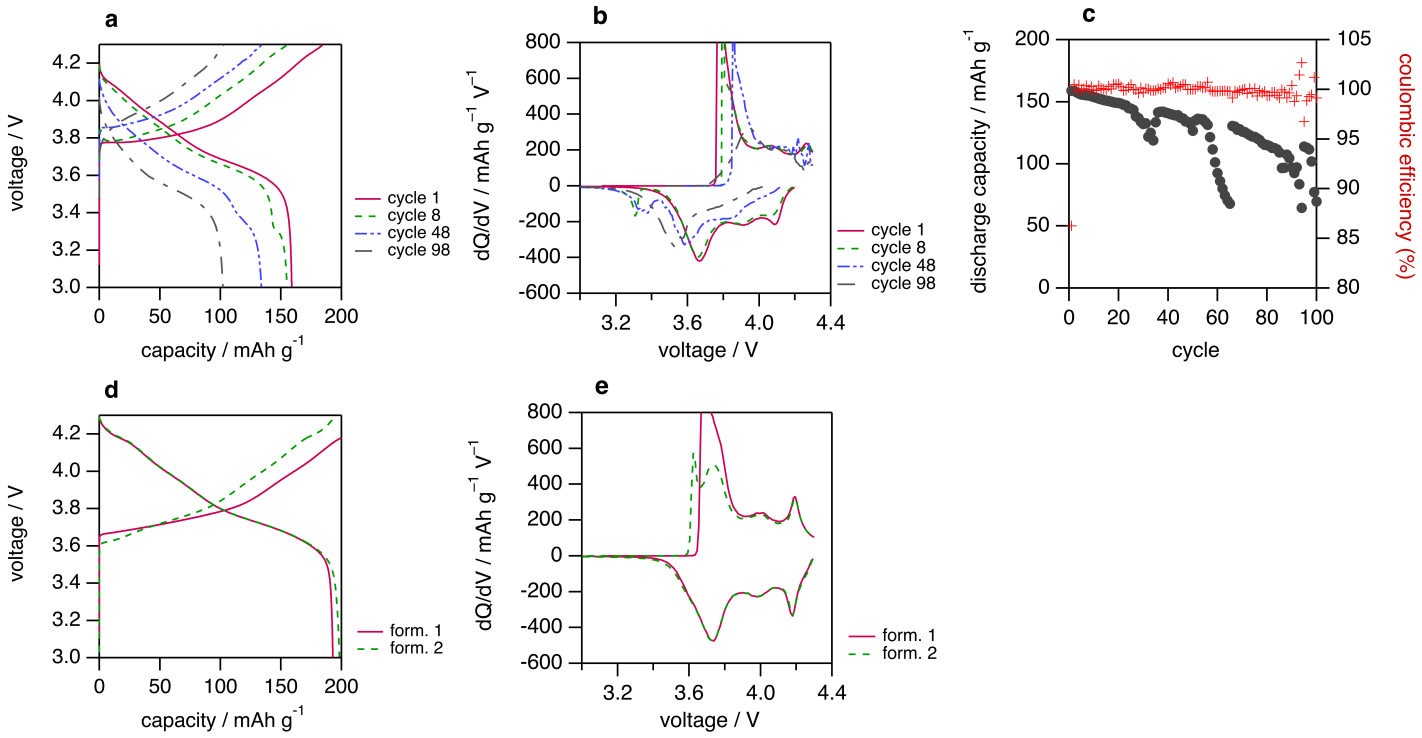

Figure 31 Electrochemical performance for cell H180c (see Table 5 for composition. a) Charge and discharge curves and b) dQ/dV curves for selected cycles at 1C. c) Capacity fade over 100 cycles. d) Charge and discharge curves and e) dQ/dV curves for the two formation cycles at C/20.

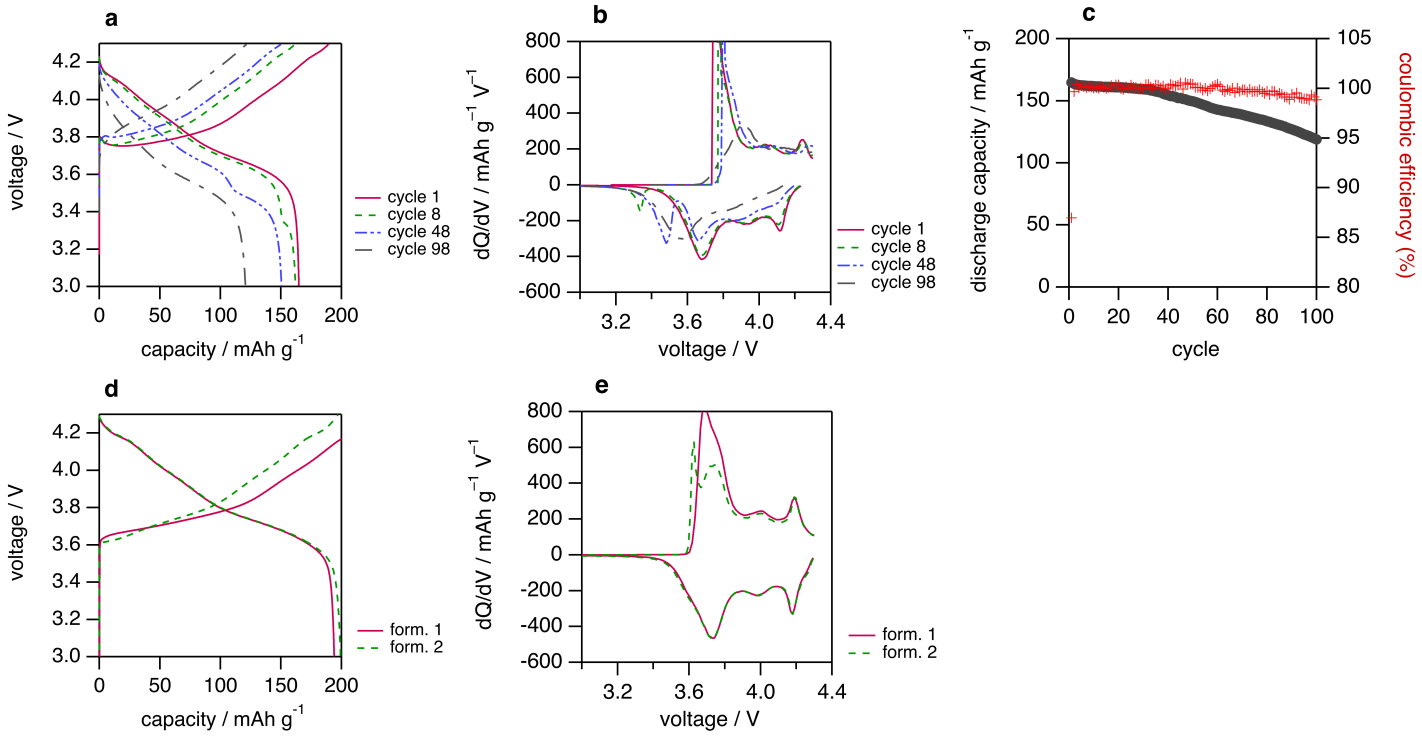

Figure 32 Electrochemical performance for cell H320a (see Table 5 for composition. a) Charge and discharge curves and b) dQ/dV curves for selected cycles at 1C. c) Capacity fade over 100 cycles. d) Charge and discharge curves and e) dQ/dV curves for the two formation cycles at C/20.

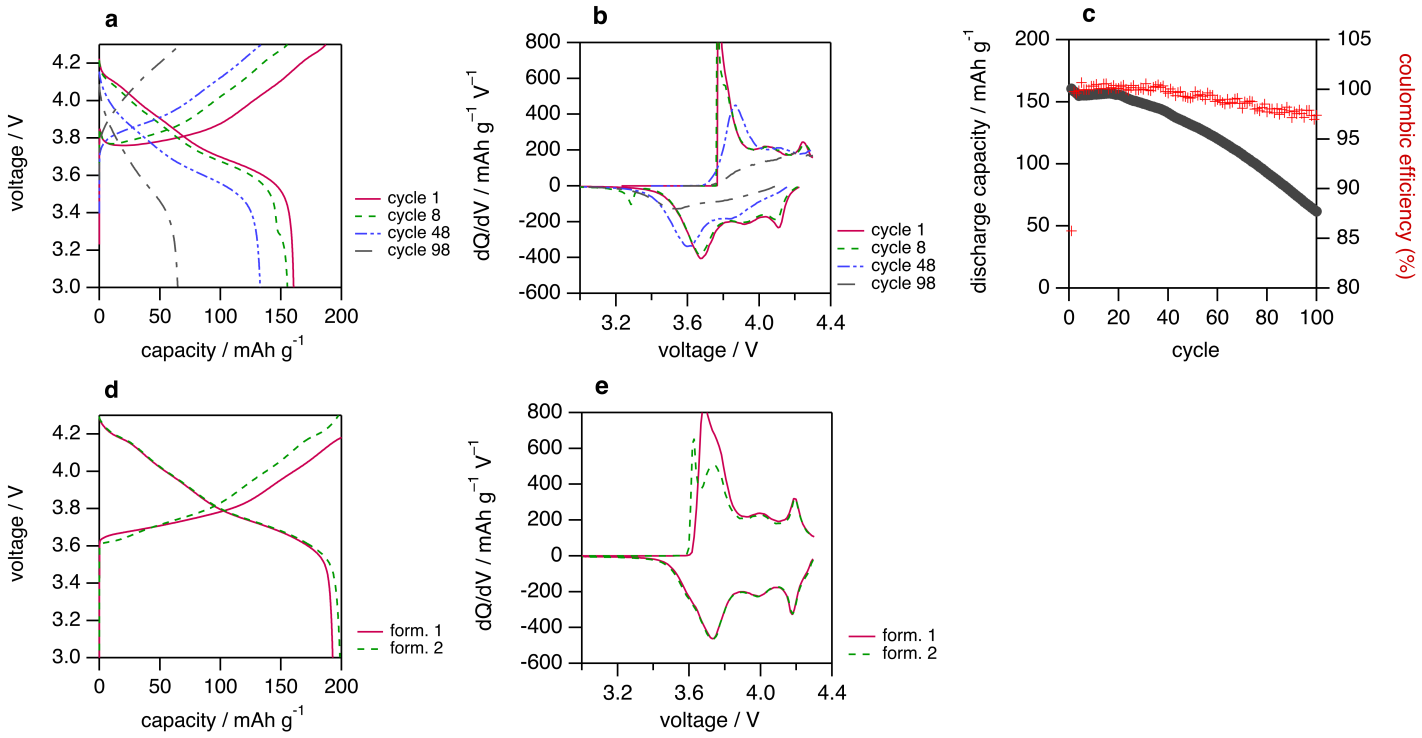

Figure 33 Electrochemical performance for cell H320b (see Table 5 for composition. a) Charge and discharge curves and b) dQ/dV curves for selected cycles at 1C. c) Capacity fade over 100 cycles. d) Charge and discharge curves and e) dQ/dV curves for the two formation cycles at C/20.

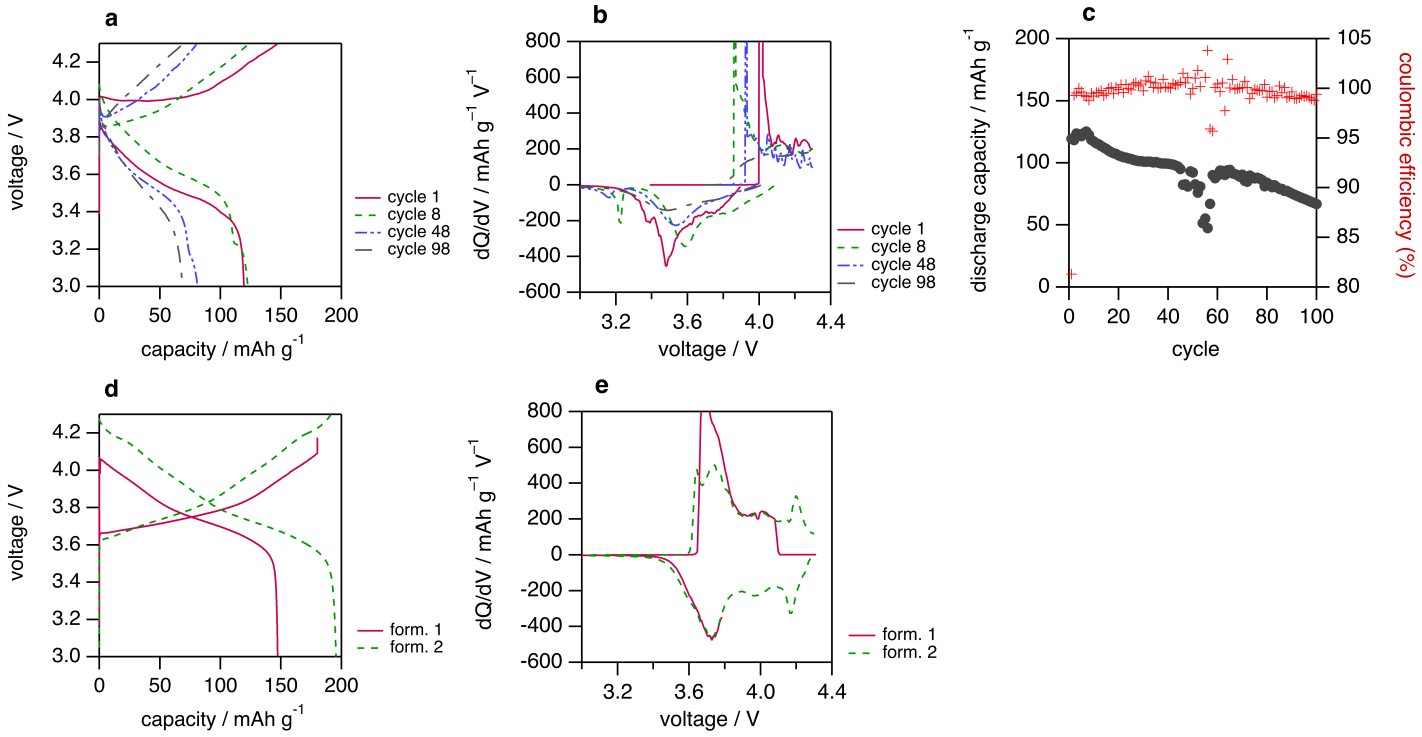

Figure 34 Electrochemical performance for cell H320c (see Table 5 for composition. a) Charge and discharge curves and b) dQ/dV curves for selected cycles at 1C. c) Capacity fade over 100 cycles. d) Charge and discharge curves and e) dQ/dV curves for the two formation cycles at C/20.

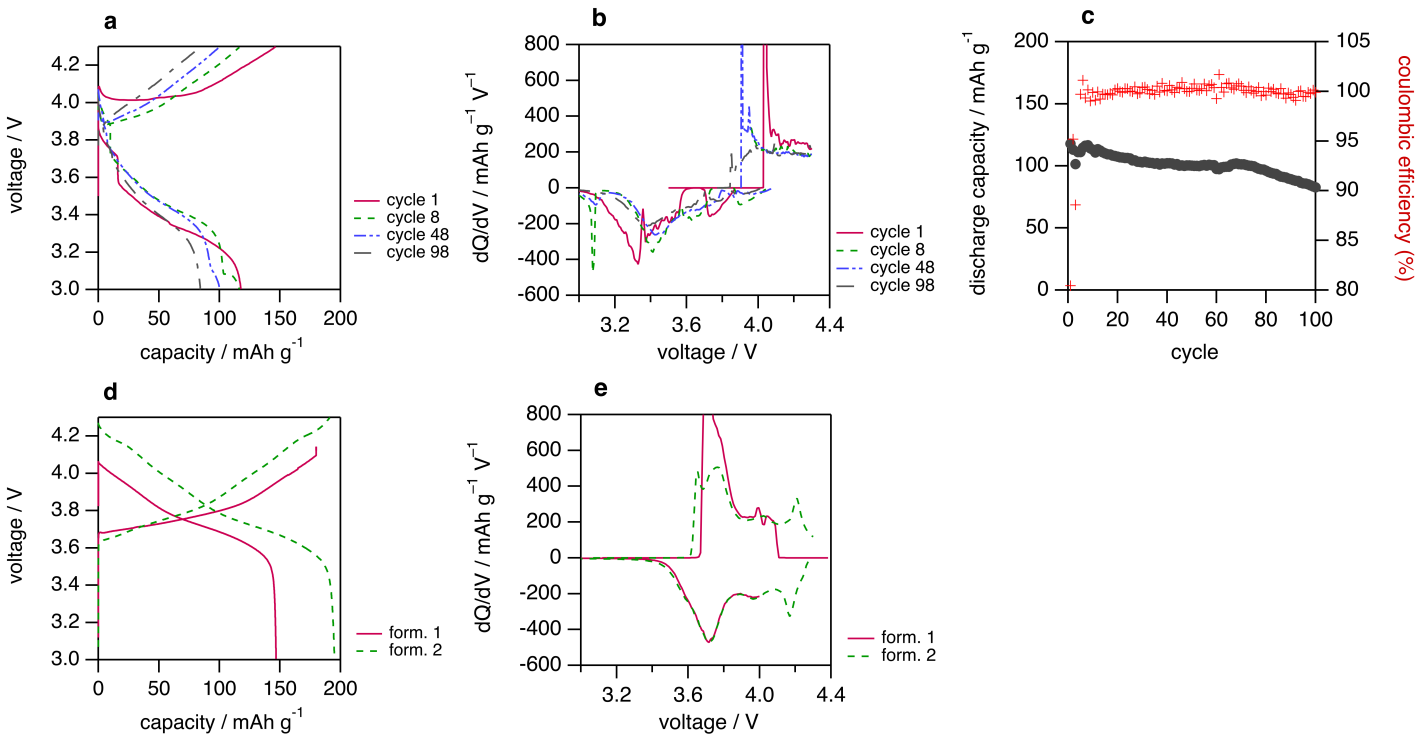

Figure 35 Electrochemical performance for cell H320d (see Table 5 for composition. a) Charge and discharge curves and b) dQ/dV curves for selected cycles at 1C. c) Capacity fade over 100 cycles. d) Charge and discharge curves and e) dQ/dV curves for the two formation cycles at C/20.

Notes and references

[1] C. D. Reynolds, S. D. Hare, P. R. Slater, M. J. H. Simmons and E. Kendrick, *Energy Technology*, 2022, **10**, 2200545.

[2] M. E. Spahr, D. Goers, A. Leone, S. Stallone and E. Grivei, *Journal of Power Sources*, 2011, **196**, 3404–3413.

[3] G. Lutringer and G. Weill, *Polymer*, 1991, **32**, 877–883.

[4] M. Okabe, R. Wada, M. Tazaki and T. Homma, *Polymer Journal*, 2003, **35**, 798–803.

[5] H. A. Barnes, *Journal of Non-Newtonian Fluid Mechanics*, 1999, **81**, 133–178.

[6] Targray, *NMC811 Powder Specifications*, https://www.targray.com/li-ion-battery/cathode-materials/nmc.

[7] Sigma–Aldrich, *Safety Data Sheet for 1-Methyl-2-pyrrolidinone*.

[8] J. Richardson and W. Zaki, *Chemical Engineering Science*, 1954, **3**, 65–73.